Atmos. Chem. Phys. Discuss., 6, 6957–7050, 2006
www.atmos-chem-phys-discuss.net/6/6957/2006/

Atmospheric Chemistry and Physics Discussions

The atmospheric chemistry general circulation model ECHAM5/MESSy1: consistent simulation of ozone from the surface to the mesosphere

P. Jöckel[1], H. Tost[1], A. Pozzer[1], C. Brühl[1], J. Buchholz[1], L. Ganzeveld[1], P. Hoor[1], A. Kerkweg[1], M. G. Lawrence[1], R. Sander[1], B. Steil[1], G. Stiller[2], M. Tanarhte[1], D. Taraborrelli[1], J. van Aardenne[1,*], and J. Lelieveld[1]

[1]Max Planck Institute for Chemistry, Atmospheric Chemistry Department, P.O. Box 3060, 55020 Mainz, Germany
[2]Institute for Meteorology and Climate Research, Forschungszentrum Karlsruhe, P.O. Box 3640, 76021 Karlsruhe, Germany
[*]now at: European Commission, DG Joint Research Centre, Ispra, Italy

Received: 23 June 2006 – Accepted: 7 July 2006 – Published: 25 July 2006

Correspondence to: Patrick Jöckel (joeckel@mpch-mainz.mpg.de)

Abstract

The new Modular Earth Submodel System (MESSy) describes atmospheric chemistry and meteorological processes in a modular framework, following strict coding standards. It has been coupled to the ECHAM5 general circulation model, which has been slightly modified for this purpose. A 90-layer model version up to 0.01 hPa was used at T42 resolution (≈2.8° latitude and longitude) to simulate the lower and middle atmosphere. The model meteorology has been tested to check the influence of the changes to ECHAM5 and the radiation interactions with the new representation of atmospheric composition. A Newtonian relaxation technique was applied in the tropospheric part of the domain to weakly nudge the model towards the analysed meteorology during the period 1998–2005. It is shown that the tropospheric wave forcing of the stratosphere in the model suffices to reproduce the Quasi-Biennial Oscillation and major stratospheric warming events leading e.g. to the vortex split over Antarctica in 2002. Characteristic features such as dehydration and denitrification caused by the sedimentation of polar stratospheric cloud particles and ozone depletion during winter and spring are simulated accurately, although ozone loss in the lower polar stratosphere is slightly underestimated. The model realistically simulates stratosphere-troposphere exchange processes as indicated by comparisons with satellite and in situ measurements. The evaluation of tropospheric chemistry presented here focuses on the distributions of ozone, hydroxyl radicals, carbon monoxide and reactive nitrogen compounds. In spite of minor shortcomings, mostly related to the relatively coarse T42 resolution and the neglect of interannual changes in biomass burning emissions, the main characteristics of the trace gas distributions are generally reproduced well. The MESSy submodels and the ECHAM5/MESSy1 model output are available through the internet on request.

1 Introduction

Ozone plays a key role in atmospheric chemical and radiation processes and for the existence of the stratosphere. The meridional gradients in solar radiation absorption by ozone drive the stratospheric circulation, and ozone photochemistry drives oxidation mechanisms in both the stratosphere and troposphere. In the past, atmospheric chemistry general circulation models (GCMs) generally focused either on the lower or middle atmosphere, addressing e.g. global photo-oxidant formation or ozone depletion, respectively (Roelofs and Lelieveld, 2000; Steil et al., 2003). However, it is becoming increasingly evident that the understanding of links between these vertical layers up to the mesosphere may be central in improving our ability to model atmospheric composition, weather and climate (Pawson et al., 2000; Austin et al., 2003).

The intricate coupling of numerical schemes for different parts of the atmosphere and the replacement of prescribed boundary conditions by process descriptions introduces additional feedback mechanisms, while the options to tune the GCMs towards the observed state of the atmosphere decrease. On the other hand, the increasing complexity of GCMs can impede the error analyses and increase the vulnerability to numerical problems. Therefore, the further development towards Earth system models requires advanced methodologies to optimally use the growing availability of computing power.

We present a new coupled lower-middle atmospheric chemistry model, linked to the 5th generation European Centre Hamburg GCM, ECHAM5 (Roeckner et al., 2003, 2004). We pursue a rigorous modularisation and apply coding standards to face the challenges associated with increasing model complexity (Jöckel et al., 2005). The resulting Modular Earth Submodel System (MESSy) is portable, user-friendly and flexible, well-documented and easily expandable (see http://www.messy-interface.org). The system enables the testing of different modules of the same processes (e.g. convection) under otherwise identical numerical conditions. Similar to the ECHAM5 model, MESSy will be publicly available for non-commercial applications through the above

mentioned web-site with the only requirement that users report results and share model advancements.

We have developed many new or improved atmospheric chemistry modules, as presented in the next section. In subsequent sections we present the first comprehensive use of ECHAM5/MESSy to simulate tropospheric and stratospheric ozone. We have compared the results to in situ and satellite measurements, with an emphasis on meteorological and transport characteristics of the coupled model. The tested meteorological parameters include temperature and moisture to ensure that the new modules do not deteriorate the ECHAM5 simulations of dynamical and physical processes that influence the chemical weather. We furthermore focus on chemical parameters for which extensive data sets are available, with an emphasis on tracer transport and gas-phase chemistry. For the stratosphere we used newly available satellite data. Follow-up articles address in more detail the atmospheric multiphase chemical processes involved, and the combined set of articles will be submitted to a special issue of Atmospheric Chemistry and Physics.

Our atmospheric chemistry GCM can be used to simulate both the weather and climate, the latter being the statistical representation of the former. Here we focus on the chemical weather of the period 1998–2005 based on a trace gas emission data set representative of the year 2000 (van Aardenne et al., 2005; Ganzeveld et al., 2006). The GCM is "nudged" toward realistic meteorology over this period by the assimilation of data from the European Centre for Medium-range Weather Forecasting (ECMWF) through the Newtonian relaxation of four prognostic model variables: temperature, divergence, vorticity and the logarithm of surface pressure (van Aalst et al., 2004). Apart from the prescribed sea surface temperature (SST) and the nudged surface pressure, the nudging is applied in the free troposphere, tapering off towards the surface and lower stratosphere, so that the stratospheric dynamics are calculated freely and possible inconsistencies between the boundary layer representations of the ECMWF and ECHAM5 models are avoided.

After a description of the model system and the simulation setup (Sect. 2), we first

evaluate basic characteristics of the simulated meteorology (Sect. 3) in troposphere (Sect. 3.1) and the middle atmosphere (Sect. 3.2). This is followed by an analysis of the simulated ozone, first from a global perspective (Sect. 4). Then, we compare in more detail the simulated ozone chemistry (including other important chemical compounds) in the troposphere (Sect. 5) and in the stratosphere (Sect. 6) with observations. Finally, we summarise the overall model characteristics (Sect. 7).

2 Model description and setup

ECHAM5/MESSy version 1.1 (further denoted as E5/M1) is the first implementation of an atmospheric chemistry GCM following the MESSy standard (Jöckel et al., 2005). Version 5.3.01 of ECHAM5 (Roeckner et al., 2003, 2006; Manzini et al., 2006; Roesch and Roeckner, 2006; Wild and Roeckner, 2006; Hagemann et al., 2006) serves as the basemodel layer. The modifications and additions applied to ECHAM5 are listed in Appendix A. Via the MESSy interface structure the following MESSy submodels are coupled to the system:

CLOUD contains the original cloud process and cover routines from ECHAM5 in a modularised, MESSy – conform structure and calculates the cloud microphysics, cloud distribution, and precipitation.

CONVECT calculates the process of convection. Different convection schemes can be selected. At present the original ECHAM5 convection routines (Tiedtke, 1989; Nordeng, 1994) with three types of closure (Nordeng, Tiedtke, Hybrid) are implemented. In this study, we exclusively apply the Tiedtke – Nordeng configuration, which is the default for the ECHAM5 model. The CONVECT submodel also includes an update for positive definite tracer transport (Brinkop and Sausen, 1996), which is, however, not used in this study, since convective tracer transport is calculated by the submodel CVTRANS.

CVTRANS calculates the transport of tracers as caused by convection. It uses a monotonic, positive definite and mass conserving algorithm following the bulk approach

as described in Lawrence and Rasch (2005).

DRYDEP (Kerkweg et al., 2006a) calculates gas phase and aerosol tracer dry deposition according to the big leaf approach.

H2O defines H_2O as a tracer, provides its initialisation in the stratosphere and mesosphere from satellite data, and controls the feedback with specific humidity of the basemodel. The water vapour source of methane oxidation in the stratosphere (and mesosphere) can be accounted for by using the water vapour tendency of a chemistry submodel (e.g., MECCA, as applied in the present study), or by using a satellite climatology (UARS/HALOE) of methane together with monthly climatological conversion rates pre-calculated from a MAECHAM4/CHEM simulation (Steil et al., 2003).

HETCHEM calculates heterogeneous reaction rates on stratospheric nitric acid trihydrate (NAT), ice, super-cooled ternary solutions (STS), and on stratospheric and tropospheric (sulfate) aerosols. It can easily be coupled by namelist to aerosol modules, which then provide the aerosol parameters. Monthly climatologies of stratospheric H_2SO_4 mixing ratios for the years 1960 to 1999 (derived from the Stratospheric Aerosol and Gas Experiment (SAGE) data) and tropospheric sulfate aerosol surface for present day conditions (Kerkweg, 2005) are provided, so that HETCHEM can be used in a minimum configuration to simulate reactions on sulfate aerosol (e.g. $N_2O_5 + H_2O \rightarrow 2HNO_3$). The reaction rates in the polar stratosphere are similar to the rates calculated by the PSC submodel. In the present study the H_2SO_4 climatology (monthly averages) of the year 1999 has also been used for 2000–2005 in the stratosphere.

JVAL, following Landgraf and Crutzen (1998), provides online calculations of photolysis rate coefficients (J-values) using cloud water and ice content, cloudiness calculated by the basemodel, and climatological aerosol. For ozone the prognostic tracer O_3 is used, but it is also possible to run the module with prescribed climatological ozone. A delta-two-stream-method is used for 8 spectral intervals in the UV and visible spectrum together with pre-calculated effective cross-sections (partially temperature and pressure dependent) for more than 50 tropospheric and stratospheric species. If used

for the mesosphere, Ly-alpha radiation is also included. Optionally the rates of heating through solar UV-C absorption by ozone and oxygen are calculated. This feature, however, has not been applied in this study.

LNOX is used to calculate the NO_x production resulting from lightning activity. The submodel comprises two alternative parameterisations of lightning–NO_x production (Grewe et al., 2001; Price and Rind, 1994). The latter is applied in the present study. Both approaches can be combined with the vertical C-shape distribution of Pickering et al. (1998) stretched or squeezed to the depth of the convective column, with separate parameters for continental and marine convective columns. The total lightning–NO_x production scales with the flash frequency and the amount of produced NO_x per single flash. In the present simulation, these parameters have been scaled to achieve a global lightning–NO_x production of ≈2Tg(N)/year.

MECCA, the Module Efficiently Calculating the Chemistry of the Atmosphere (Sander et al., 2005), calculates tropospheric and stratospheric chemistry. The KPP (Kinetic Preprocessor) software (Sandu and Sander, 2006) is used for the integration of the set of stiff differential equations. In the present study, the selected mechanism comprises 104 gas phase species (including H_2O defined by the submodel H2O) and 245 reactions. It comprises the O_3-related chemistry of the troposphere, including non-methane-hydrocarbons (NMHCs) up to isoprene (von Kuhlmann et al., 2003b). For the stratosphere, the main chlorine (Steil et al., 1998) and bromine (Meilinger, 2000) reactions are considered. Details of the selected chemical mechanism (including reaction rate coefficients and references) can be found in the electronic supplement (http://www.atmos-chem-phys-discuss.net/6/6957/2006/acpd-6-6957-2006-supplement.zip). The set of ordinary differential equations (ODEs) describing the chemical mechanism has been integrated in the entire model domain without artificial or arbitrary boundary- or interface conditions. MECCA uses heterogeneous rate coefficients calculated by HETCHEM and photolysis rates calculated by JVAL.

OFFLEM (Kerkweg et al., 2006b) reads surface emission fluxes (2-D), multi-layer emission fluxes (Nx2-D) and volume emission fluxes (3-D) from prescribed data files

via the MESSy data import interface (Jöckel, 2006), and either calculates tracer tendencies (2-D, 3-D, Nx2-D) or modifies the vertical diffusive flux boundary condition of the respective species at the surface (2-D only). Furthermore, OFFLEM is used to import data (Jöckel, 2006) for use in other submodels (e.g., TNUDGE). For the present study the emissions of NO, CO, C_2H_4, C_2H_6, C_3H_6, C_3H_8, C_4H_{10}, CH_3CHO, CH_3COCH_3, CH_3COOH, CH_3OH, HCHO, HCOOH, MEK, SO_2, and NH_3 are distributed as multi-layer emissions onto 6 levels (45, 140, 240, 400, 600, 800 m). The emissions comprise the anthropogenic emissions from the EDGAR3.2FT 2000 ("fast-track")[1] database and additional biogenic emissions as described in Ganzeveld et al. (2006). The aircraft NO emissions (1995) (Schmitt and Brunner, 1997) are distributed as volume emissions.

ONLEM (Kerkweg et al., 2006b) calculates surface emission fluxes for gas-phase (and optionally aerosol) tracers and either calculates tracer tendencies, or modifies the vertical diffusive flux boundary condition of the respective species at the surface. With the latter approach, emissions of DMS from the ocean, isoprene from plants, and NO from soils have been calculated. For the present simulations, the isoprene and soil NO emission fluxes have been scaled by a factor of 0.6 to achieve total net emissions of approximately 315 Tg(C)/year and 7 Tg(N)/year, respectively.

PSC, the Polar Stratospheric Cloud submodel (Buchholz, 2005), simulates microphysical processes that lead to the formation of super-cooled ternary solutions (STS), nitric acid trihydrate (NAT), and ice particles in the polar stratosphere, as well as heterogeneous chemical reaction coefficients of halogens and dinitrogen pentoxide on liquid and solid aerosol particles. Denitrification and dehydration due to sedimenting solid PSC particles are calculated for each grid box depending on particle size, pressure and temperature. PSC defines the additional tracer HNO_3_nat.

PTRAC is used to define and initialise additional tracers which are not part of the chemical mechanism. In the present study we defined SF_6 for the evaluation of the upper troposphere/lower stratosphere (UTLS) transport, and $SO_4^{(cs)}$ as a pseudo aerosol tracer (coarse mode, soluble) for closure of the SCAV mass balance.

[1] http://www.mnp.nl/edgar/model/v32ft2000edgar/docv32ft2000

QBO is a submodel for the assimilation of quasi-biennial oscillation (QBO) zonal wind observations (Giorgetta and Bengtsson, 1999; Naujokat, 1986). The QBO submodel can be used to enforce artificially the QBO in a GCM that does not simulate the QBO by internal forcing, or to synchronise an internally generated QBO with an external QBO time series. Here, the QBO submodel was used to initialise the QBO during the first year of the simulation.

RAD4ALL is a re-implementation of the ECHAM5 radiation code according to the MESSy standard. New and extended features are: (1) Choice between standard ECHAM5 radiation and RAD4ALL; (2) All input quantities are now controlled via the user interface; (3) Online coupling of radiation with trace gases; (4) All input quantities (except aerosols in the current version) can be read from external climatologies. In the present study, RAD4ALL is coupled to the prognostic cloud cover, cloud water, and cloud ice (all from CLOUD), to the prognostic specific humidity, and to the prognostic trace gases CO_2, CH_4, O_3, N_2O, F11, and F12. For the aerosol-radiation interaction, the standard ECHAM5 aerosol climatology (Tanre et al., 1984) has been applied.

SCAV simulates the processes of wet deposition and liquid phase chemistry in clouds and precipitation. It considers gas phase and aerosol species in large-scale as well as in convective clouds and precipitation events. A detailed description can be found in Tost et al. (2006). In the present study the chemical mechanism comprises 6 additional species and 41 reactions. These chemical reactions are decoupled from the comprehensive gas phase chemical reaction set of the MECCA submodel, because for some applications a relatively comprehensive and computationally expensive solver for the stiff set of ODEs is required. Details of the selected aqueous phase chemical mechanism (including reaction rate coefficients and references) can be found in the electronic supplement (http://www.atmos-chem-phys-discuss.net/6/6957/2006/acpd-6-6957-2006-supplement.zip).

SEDI calculates sedimentation of aerosol particles and their components (Kerkweg et al., 2006a). The submodel comprises a zero-order scheme (used in this study), and a first order trapezoid scheme with corrections above/below local extrema. Both

schemes are mass conserving and allow non-monotonic redistribution, as required for a correct representation of particle sedimentation.

TNUDGE (Kerkweg et al., 2006b) is used for the relaxation (nudging) of user-defined tracers with arbitrary user-defined fields (e.g., imported via OFFLEM). In the present study, TNUDGE is used to prescribe the lower boundary conditions of N_2O, CH_4, $CFCl_3$, CF_2Cl_2, CH_3CCl_3, CCl_4, CH_3Cl, CH_3Br, CF_2ClBr, CF_3Br, H_2, CO_2, and SF_6 from observed mixing ratios using the AGAGE database (Prinn et al., 2000). As in Steil et al. (2003) other source gases contributing to stratospheric chlorine, such as $C_2F_3Cl_3$, CHF_2Cl and $C_2H_3FCl_2$, are included as pseudo CF_2Cl_2 taking into account their chlorine atom number. The pseudo-fluxes resulting from the nudging tendency are diagnosed. The nudging is applied every model time step with a nudging time coefficient for all species of 3 h.

TRACER is a generic MESSy submodel and handles the data and meta-data for chemical species. Note that the current implementation is independent from a similar approach contained in ECHAM5. TRACER contains two additional sub-submodels, TRACER_FAMILY for transporting user-defined tracer-sets as tracer families, and TRACER_PDEF to force positive definite tracer mixing ratios including tracer mass diagnostics. In the present study, the following tracer families have been transported:

- ClO_X = Cl + ClO + HOCl + OClO + 2 Cl_2O_2 + 2 Cl_2
- BrO_X = Br + BrO + HOBr + BrCl + 2 Br_2
- NO_Z = N + NO + NO_2 + NO_3 + 2 N_2O_5

TROPOP diagnoses the tropopause according to various definitions. In the present study the tropopause is defined according to the WMO definition (WMO, 1992) based on the temperature lapse rate for latitudes equatorward of 30°, and as the potential vorticity iso-surface of 3.5 PVU at latitudes poleward of 30°. Moreover, TROPOP diagnoses the height of the planetary boundary layer for several applications.

Additional and alternative submodels are also included in MESSy version 1.1; they are not applied in the present study and are listed in Appendix B. The coupling among the various submodels and to the basemodel is sketched in Fig. 1.

The following submodels provide a coupling between chemistry and dynamics:

- RAD4ALL: Radiative temperature tendencies are calculated depending on the tracers CO_2, CH_4, O_3, N_2O, F11, and F12, and depending on the cloud cover (calculated by CLOUD), the water vapour, the cloud water content, and cloud ice.
- H2O: The chemical H_2O tendency calculated by MECCA is fed back to the specific humidity of the basemodel.
- PSC and HETCHEM: These submodels calculate the partitioning of total water into water vapour, liquid water, and ice, within and outside the PSC regions, respectively.
- CLOUD: Cloud droplet formation changes the partitioning of total water into vapour, liquid and ice.
- CONVECT: Water vapour, liquid water, and ice are transported by convection.

The model simulations have been performed for the period January, 1998, to October, 2005, in T42L90MA resolution (MAECHAM5, Giorgetta et al., 2002, 2006), i.e., with a triangular truncation at wave number 42 for the spectral core of ECHAM5, and with 90 levels on a hybrid-pressure grid in the vertical, reaching up to 0.01 hPa (middle of upper layer). The vertical resolution near the tropopause is about 500 m. The corresponding model time step is 900 s. Output has been archived as 5-hourly instantaneous fields to capture an hourly resolved diurnal cycle within 5 days of integration. The high vertical resolution has been chosen to overcome problems in the representation of stratosphere to troposphere exchange (as identified by models with lower vertical resolution), and for being able to simulate the QBO effects on chemistry directly.

To represent the observed meteorology in the troposphere, ECHAM5 has been nudged (Jeuken et al., 1996) towards analysis data from the ECMWF operational forecast model. The nudging of temperature, surface pressure, divergence, and vorticity (in spectral representation) was applied between model levels 63 (≈97 hPa) and 84 (≈706 hPa), with additional transition zones (intermediate stepwise reduced nudging coefficients) between levels 58 (≈62 hPa) and 62 (≈89 hPa), and 85 (≈775 hPa) and 87 (≈909 hPa). The namelist with nudging coefficients can be found in the electronic supplement (http://www.atmos-chem-phys-discuss.net/6/6957/2006/acpd-6-6957-2006-supplement.zip).

In addition to the reference simulation (further denoted as S1) described so far, a sensitivity simulation (further denoted as S2) encompassing the period 2002 to 2005 with the following changes has been performed: Starting from January 2002 of the S1 simulation, the nudging has been reduced in the vertical down to level 71, i.e., to approximately 204 hPa, with a transition zone from level 65 (≈116 hPa) to 70 (≈185 hPa). From March 2003 onward, the gravity wave forcing (Hines, 1997a,b; Manzini and McFarlane, 1998) has been reduced by decreasing the root mean square gravity wave wind speed at the launching height from 1 m/s to 0.9 m/s (Giorgetta et al., 2006). From July 2004 onward, the time step has been reduced to 600 s. Finally, in September/October 2005 the QBO nudging (discussed below) has been switched on again. The simulations have been performed on the IBM pSeries "Regatta" system based on Power 4 processor technology at the Max Planck "Rechenzentrum Garching" (RZG). We used 16 compute nodes with 256 CPUs in total.

3 Meteorology

3.1 The hydrological cycle: precipitation and water vapour

An accurate representation of the hydrological cycle is crucial for the accurate modeling of the meteorology in a climate-chemistry model. Hagemann et al. (2006) have per-

formed a detailed evaluation of the hydrological cycle of ECHAM5 using free-running simulations at different resolutions and observed climatologies of precipitation, evaporation and river runoff. The T42L90MA resolution used here was not considered by Hagemann et al. (2006), nor did they perform any nudged simulations. In this section we show that with the modifications introduced by the MESSy system and the coupling between chemistry and climate, as well as by the application of the T42L90MA resolution and nudging, the simulation produces a hydrological cycle consistent with observations. We examine two key parameters of the hydrological cycle, water vapour column (WVC) and precipitation, for boreal winter (DJF) and boreal summer (JJA) for the time period 1999–2002 for which satellite data are available. Note that precipitation and WVC are most relevant through the links between the hydrological cycle and HO_x chemistry, dry and wet deposition, and emissions.

Observational data sets

Observational data sets used for the model evaluation are the Global Precipitation Climatologies Project (GPCP) (Huffman et al., 1997; Rudolf, 2001) for precipitation, and the merged data set combining GOME (Global Ozone Monitoring Experiment) and SSM/I (Special Sensor Microwave/Imager) for the WVC. The GPCP data set contains estimates from satellite observations and data from about 7000 geolocations over land surfaces. These estimates have relatively large uncertainties over the ocean (Adler et al., 2001). WVC data are provided by GOME over cloud-free land and ocean and by SSM/I in the cloudy pixels over ocean. A detailed description of these datasets including all relevant references can be found in Lang and Lawrence (2005a,b).

Zonal averages

Figure 2 shows the zonal distribution of simulated and observed precipitation for boreal winter (DJF) and boreal summer (JJA).

Although the shape of the zonal distribution resembles the shape of the GPCP distri-

bution quite well in the winter season, the model mean precipitation maximum around 15° S is about 2 mm/day higher than the GPCP data. Also, this peak is broader in comparison to the GPCP data. For the subtropical minimum in the southern hemisphere the model is lower by about 1 mm/day at 35° S compared to the observations. The distribution in the northern hemisphere compares very well in shape and in absolute values with observations. In summer, the model peaks with higher values at 10° N. Additionally, the precipitation maximum in the tropics is broader in the model simulation, resulting in an overall overestimation. The model results show a small increase in the zonal average at about 30°N which is not observed. This is related to the overestimation of precipitation by the model in the Himalaya region (compare also the upper left panel of Fig. 4). On the other hand, the GPCP double peak at 40° S and 60° S is not captured by the model. In the northern hemisphere the model precipitation is slightly overestimated poleward of about 45° N.

Figure 3 shows the zonal distribution of the water vapour column, again for boreal winter and boreal summer.

The general shape of the model results and the observations is quite similar. In boreal winter, the model water vapour is underestimated between 10° S and 5° N and slightly overestimated elsewhere. In summer, the model WVC is slightly higher than GOME in the northern hemisphere (between 40° N and 70° N). In the tropics the zonal distribution is very similar to the observations, while south of 20° S a significant overestimation (more than 40%) by the model occurs. Due to the lack of observations a comparison in the polar regions is not feasible.

Geographic distributions

The model produces a relatively high globally averaged precipitation rate compared to GPCP for the time period 1999–2002 (global model mean: 3.0 mm/day, global GPCP mean: 2.6 mm/day, i.e., a bias of 0.4 mm/day, Root Mean Square (RMS): 1.3 mm/day). A slightly high global WVC compared to GOME/SSMI data, is also simulated (global model mean: 2.44 cm, global GOME/SSMI mean: 2.34 cm, bias:

0.095 cm, and RMS: 0.32 cm).

The left column of Fig. 4 shows a comparison of the annually averaged simulated and observed precipitation climatologies for the period 1999 to 2002.

The basic patterns of precipitation are well captured. However, the model significantly overestimates the observations in the tropics (Brazil, central Africa, Central America, the Indian Ocean and the western Pacific warm pool) and China. The model precipitation rate is also too high along steep mountains (Tibet, Andes) and along the Southern Pacific Convergence Zone (SPCZ). On the other hand, the precipitation is slightly underestimated in the central Pacific and central Atlantic ITCZ. In the mid-latitudes the oceans are characterised by a slight underestimation of the model, while over the continents the precipitation distribution is captured well in shape and strength. We note that data coverage over the oceans and remote continental areas (e.g., mountains) is relatively poor, so that these data-model discrepancies may not be significant.

The right column of Fig. 4 shows the annual average global water vapour column (WVC) distribution as modeled by E5/M1 and as measured by GOME/SSMI for the period 1999 to 2002. The WVC gradients are modeled quite realistically by E5/M1 from the moist regions over the ITCZ to the dry regions at the poles. In the mid-latitudes of both hemispheres the model overestimates the WVC over the ocean. Even though the regions with major evaporation are located closer to the equator, an overestimation of local evaporation cannot be completely excluded. The simulated precipitation in these regions is slightly lower compared to the observations, however, the differences can hardly explain the higher WVC values. Furthermore, water vapour can be transported into the mid-latitude storm tracks too efficiently, mainly close to the surface. Over the dry regions of Arabia and the Sahel the model significantly underestimates the observed WVC. This can partly be attributed to higher observed values resulting from hygroscopic aerosols which deteriorate the retrieval algorithm (Lang and Lawrence, 2005b). In the region with higher observed values than simulated by the model in the tropical ITCZ the results are self-consistent, since the model calculates higher precipitation in these regions. The WVC over the mid-latitude continents is in close agreement

with the observed values.

One additional issue we have come across with respect to the model nudging is that for the dry season in the Amazon region the moisture divergence over the forest seems too strong, which can give rise to local runaway drying. In the S1 simulation based on the assimilation of ECMWF data the precipitation over the Amazon is unrealistically low, resulting in soil drying and suppression of evapotranspiration and cloud formation. A consequence of this is that the isoprene emissions, which depend on temperature, are biased high in this region during the dry season; the causes and further implications of this phenomenon are being investigated in follow-up studies. In a test simulation in which only ECMWF temperature and surface pressure data have been assimilated (SST prescribed) this problem did not occur. Further testing at different resolutions will be necessary to identify the specific cause, which could be related to the nudging procedure (Bengtsson et al., 2004) as well one of the routines that affect the hydrological cycle.

Overall, the hydrological cycle is reproduced rather realistically in the E5/M1 simulation. Even though there are some discrepancies with the observed precipitation and WVC, these results of E5/M1 are in good agreement with the analysis of the hydrological cycle evaluated in Hagemann et al. (2006), who also show a precipitation overestimation in the tropics, especially the warm pool region and a similar discrepancy in the northwestern Tibet region.

3.2 Middle atmosphere

The model calculated dynamics of the middle atmosphere essentially results from the model integration alone. The assimilation of the weather in the troposphere includes waves that propagate vertically and dissipate in the middle atmosphere, driving zonal and meridional circulations. Phenomena in the stratosphere and mesosphere that are sensitive to such wave forcing are therefore indirectly controled by the assimilation in the troposphere. Examples are the QBO and sudden or major warmings. This does not imply that the stratosphere is a slave to the tropospheric waves only, since wave

propagation from the troposphere to the stratosphere also depends on the state of the stratosphere. Therefore, we do not expect the simulated stratosphere to always and everywhere follow the observations, but rather that the major phenomena that depend on vertically propagating waves are simulated realistically. In addition, we expect to reproduce features which are only weakly dependent on the dynamics, for example ozone concentrations in regions where radiative and chemical time scales are much shorter than the transport time scale.

3.2.1 Temperatures compared to satellite data

The Michelson Interferometer for Passive Atmospheric Sounding (MIPAS) on the ENVISAT satellite provides 19 months of profiles of temperatures and several chemical constituents with global coverage during day and night (von Clarmann et al., 2003a). For evaluation we use here the products of a scientific processor by von Clarmann et al. (2003b). For a systematic comparison with the MIPAS satellite observations, simulated temperature profiles have been subsampled from the model output at the same location and local time as the satellite observations. This approach is feasible because of the nudged tropospheric forcing. We compare averages and the variability for the 4 seasons (DJF, MAM, JJA, SON) for the period December 2002 to November 2003.

As can be seen from Fig. 5 for most regions, the agreement of the average model data with the observations is in the order of the systematic error range of the observations, i.e., within about 1–2 K (Wang et al., 2005). The cold bias in the southern winter lower-middle stratosphere, present in many GCMs (Austin et al., 2003), including the previous version of our model (Steil et al., 2003), is strongly reduced.

From a comparison of MIPAS and ECMWF temperatures for the period of mid-October to mid-November 2003 (Wang et al., 2005), it can be concluded that E5/M1 results for the stratosphere are similar in quality to the ECMWF data, although we do not assimilate observations, contrary to ECMWF. The ECMWF temperatures show no cold bias below 30 km, whereas our model simulates a slightly too cold tropical stratosphere. Between 30 and 40 km altitude in the northern hemisphere the ECMWF data

become cold biased with a deviation of up to 7 K at 50 km in the Arctic, while our model matches the MIPAS temperatures. Above 45 km the ECMWF temperatures are warm biased by 3–4 K in low and middle latitudes, whereas our model tends to underestimate temperatures in comparison with MIPAS data by 2–3 K.

The model temperatures in the polar winter and spring lower stratosphere (<10 hPa) compare quite well with MIPAS observations. For the Arctic there is no temperature bias. The mid-winter Antarctic temperatures in the lower stratosphere agree well and in spring the cold bias of 2–3 K is small. In SH midwinter above 25 hPa the model temperatures are relatively low by 3–7 K in high latitudes and 2–6 K high between 40–55° S. The low bias points to a too weak subsidence in the polar vortex (see below) whereas the warm bias indicates an extension of the vortex too far to the north, which is confirmed by too low N_2O in the simulation compared to MIPAS measurements (see below). The slightly too cold tropical stratosphere and summer mesosphere and a too warm winter mesosphere indicates deficiencies related to the heating rate calculations or adiabatic cooling / warming rates related to the model nudging. Temperatures are closer to the observations everywhere with only tropospheric nudging (up to ≈200 hPa) and weaker gravity wave forcing in simulation S2.

3.2.2 The Brewer Dobson circulation and the transport barriers

The comparison between model and satellite data for the trace gas N_2O as example for a mostly transport controlled long lived source gas has been performed in the same way as for the temperatures in the previous section (Fig. 6). For most regions the agreement between model and MIPAS is close to the observational uncertainty range of about 7% for total systematic errors (Glatthor et al., 2005b) (the effect of random error is strongly reduced due to the large dataset). The model reproduces the observed distribution in the tropics and the subtropical transport barriers well, including the features related to the QBO in the upper stratosphere, indicating that the upward branch of the Brewer Dobson circulation is simulated correctly. This holds also for methane and halocarbons (not shown here).

The largest differences occur directly poleward of the subtropical barriers (surf zone) and in the lowermost polar stratosphere in spring and winter. These are partially related to the differences in horizontal and vertical resolution of the satellite and the model data. Note that the MIPAS data is obtained by limb-scan from a polar orbit in the anti flight direction. The resolution is about 30 km in the zonal, 500 km in the meridional, and 3 km in the vertical direction (Endemann et al., 2000).

Hence differences in representing mesoscale features such as streamers (e.g. Riese et al., 1999) and even synoptic structures due to planetary waves can be expected. The gradients at the vortex edges simulated by the model are less steep than the observed. In the polar lowermost stratosphere the database is sparse because of interferences by polar stratospheric clouds and because the data have larger uncertainties due to large horizontal gradients, i.e., the differences are only partially significant. Nevertheless, the model generally seems to underestimate the downward transport in the winter lowermost polar stratosphere below about 40 hPa (Fig. 6) which causes also an underestimate of reactive halogens and ozone depletion there.

3.2.3 The Quasi-Biennial Oscillation (QBO)

In the tropics the model self-consistently calculates the quasi-biennial oscillation (QBO) of the zonal wind from 1999 to 2003. It is based on resolved waves, assimilated in the troposphere from ECMWF analysis, and parameterised gravity wave drag. With nudging only to 200 hPa in the sensitivity study S2 it stays close to the observations until the end of the simulation period in 2005 (Fig. 7).

With the nudging to ≈100 hPa, after spring 2004 the zonal winds in the lower tropical stratosphere remain in one phase, caused by a blocking layer of westerlies near the tropical tropopause.

3.2.4 The 2002 southern hemispheric major warming in the model and in satellite data

The lower stratospheric dynamics and the distribution of total ozone as observed by TOMS (Total Ozone Mapping Spectrometer; on the NASA Earthprobe satellite) is to a large extent controlled by planetary waves propagating from the troposphere. Nudging of the tropospheric meteorology enables the model to reproduce the major stratospheric warming in the Austral spring of 2002 and the remarkable vortex split in September 2002. The details in total ozone agree better with TOMS observations in the case of nudging only up to ≈200 hPa (simulation S2) instead of ≈100 hPa (simulation S1), in contrast to several previous approaches where models were forced at 100 hPa (e.g., Manney et al., 2005). As shown in Fig. 8, the two parts of the vortex are separated too strongly when also the lower stratosphere is nudged, possibly pointing to problems in the ECMWF-data in the Antarctic lower stratosphere.

The model shows a high-ozone bias (further discussed in Sect. 6.1), which decreases in the simulation with reduced nudging (S2). A detailed comparison of pressure / longitude cross sections at about 63° S intersecting the two vortex lobes with MIPAS satellite data shows that the model reproduces the vertical structure of temperatures and chemical species within the experimental uncertainties (Fig. 9). We selected the conditions one day before the full vortex split because of better data coverage compared to the conditions 4 days later for which the TOMS comparisons were performed. Figure 9 shows a slight underestimate of ozone depletion inside the vortices which might be related to an underestimate of activated ClO (for which the satellite data is not shown because it is too noisy).

The model also reproduces the observed dehydration and denitrification inside the vortices, shown here with HNO_3 and NO_2 as examples. These also show the diurnal cycles of NO_2 and ozone, which compare well with the MIPAS observations (Glatthor et al., 2005a; Mengistu Tsidu et al., 2005; Funke et al., 2005b). The experimental uncertainty for NO_2 for these "snapshots" is about 10% at night and 20% at daytime.

One has to keep in mind that the comparisons are not done exactly at the same time so that some differences can be caused just by movement of the vortex lobes with their strong gradients.

4 Global ozone distribution and budgets

4.1 Total ozone

The zonal mean total ozone for the full 8 year period (Fig. 10) as well as snapshots for several different situations in different seasons (the latter not shown) have been compared with the TOMS observations (V8, see http://jwocky.gsfc.nasa.gov).

Owing to the nudging of the tropospheric meteorology most large-scale and regional patterns observed by TOMS are reproduced in the simulations. This includes "mini-holes" in the northern hemisphere, the Antarctic ozone hole, including its remarkable split in September 2002 (see Sect. 3.2.4) and the decline of total ozone in northern high latitudes from spring to fall. Figure 11 shows the time series resulting from the simulations and observations based on 10-day zonal averages.

It can be clearly seen that the model reproduces the inter-annual and seasonal variability of observed total ozone. In the tropics calculated total ozone is very close to the observations, while in mid-latitudes and high latitudes the simulations are high by up to about 10–15%, close to the uncertainty of the satellite instrument and retrieval algorithm. For simulations S2 (2003 to 2005) the bias in middle and high latitudes is typically 20 DU less, i.e., in all cases the model results are within 10% of the measurements.

4.2 Model climatologies of ozone for the four seasons

The calculated ozone climatologies for the four seasons from the surface to the mesosphere are shown in Fig. 10. They are obtained from the periods December 1999

to November 2001 and December 2002 to November 2004. Note that the period in between is excluded because of the unusual meteorological situation associated with the southern hemispheric major stratospheric warming. Figure 10 emphasises one of the special features of this simulation: a consistent representation of O_3 chemistry in the troposphere, stratosphere, and mesosphere with no artifical boundaries. The tropospheric distribution, in particular the O_3 pollution in the northern hemisphere mid-latitudes near the surface, the low tropical O_3 throughout the column, and the stratospheric O_3 influx near the tropopause "breaks" in the spring of both hemispheres are well known features. In the stratosphere the Antarctic ozone hole and the ozone maximum around 10 hPa are well represented.

4.3 Stratospheric and mesospheric chemical ozone budgets

To derive the ozone budget, we integrated the O_3 reaction rates from the MECCA mechanism (see electronic supplement (http://www.atmos-chem-phys-discuss.net/6/6957/2006/acpd-6-6957-2006-supplement.zip)) using the 5-hourly distributions (model output) of the relevant tracers and the O_2 photolysis rate (JVAL) for the stratosphere and the troposphere (see TROPOP for the tropopause definition). For the integration in the stratosphere, we have chosen model level 37 (≈10 hPa) as an upper boundary. Table 1 shows the production from photolysis of oxygen, $NO + HO_2$ and $NO + CH_3O_2$, and the loss terms due to different catalytic cycles. In the stratosphere there is a net chemical gain of ozone which is balanced by transport to the troposphere. The individual terms contributing to the chemical ozone budget are about an order of magnitude larger in the upper stratosphere; there is, however, almost photochemical equilibrium, i.e., the large terms are mostly cancelling each other. Therefore, most of the net production and flux to the troposphere is controlled by the layers below 10 hPa. Considering the layers above reduces the net gain term by about 10%. The selection of the dynamical tropopause as the lower boundary of the integration domain has only a small influence, and the corresponding fluxes across the 100 hPa level are very similar.

Stratospheric ozone production and loss during summer is dominated by gas phase

chemistry. Furthermore the dynamical wave activity is small so that the summer conditions are most suited for validation of the scheme for homogeneous chemistry used in the GCM. In high and mid-latitudes ozone decreases from spring to fall due to catalysis by NO_x under polar daylight conditions in the altitude region between about 10 to 100 hPa (Brühl and Crutzen, 2000; Crutzen and Brühl, 2001). Net chemical ozone production as calculated by the model for the NH-summer (June and August) is depicted in Fig. 12. The results agree well with the corresponding figures in the above papers, where results were constrained by HALOE observations.

The net chemical production changes sign at the correct latitudes and altitudes. Above about 2 hPa diurnally averaged ozone is close to photochemical equilibrium. The net gain in the tropics below 10 hPa is balanced by loss to the layers above via the upward motion of the Brewer-Dobson circulation. Figure 12 also shows the corresponding terms for southern hemispheric summer. The large chemical loss due to reactive nitrogen south of 40° S explains the secondary minimum in total ozone there in March.

In the winter hemispheres the net production in the upper stratosphere is balanced by the downward motion which also reduces the ozone loss in the middle stratosphere. In the lower high latitude stratosphere, especially in the southern hemisphere, strong chemical ozone loss takes place due to catalytic destruction by halogens, peaking near the terminator.

4.4 Tropospheric ozone budgets

The tropospheric chemical ozone budget is derived in a similar way as the one for the stratosphere using the 5 hourly output of the tracers. The dry deposition of O_3 was diagnosed from the submodel DRYDEP. From these values the net stratosphere-to-troposphere (STT) flux of ozone was calculated by closure of the budget, also taking into account the upward flux in the tropics and the (negligible) change of the tropospheric O_3 burden. In addition, the chemical mechanism includes a tracer for stratospheric ozone ($O_3^{(s)}$), which has been "hard-nudged" by TNUDGE to O_3 in the strato-

sphere. In the troposphere, $O_3^{(s)}$ undergoes the same chemical loss reactions as O_3, and is also affected by dry deposition. The chemical loss has been "accumulated" over time, and was integrated offline. This chemical loss of $O_3^{(s)}$ plus its dry deposition provides a direct measure of the stratosphere-to-troposphere transport of ozone that has been produced in the stratosphere. The results of our calculations are listed in Table 2.

The results are consistent with the study by Roelofs and Lelieveld (1997) who used ECHAM4 with a simpler chemistry setup constrained by observations. In a recent multi-model inter-comparison (Stevenson et al., 2006), the net tropospheric ozone production was estimated to be P=(5110±606) Tg, with a net loss of L=(4668±727) Tg, whereby the range is the multi-model standard deviation. Furthermore, the multi-model ozone dry deposition is (1003±200) Tg, and the inferred net stratospheric influx STT=(552±168) Tg. These numbers show that the simulated tropospheric ozone budget of E5/M1 agrees well with the multi-model ensemble, whereby the dry deposition and inferred STT are near the lower end of the range in the comparison. The latter underscores the improved representation of the stratosphere-to-troposphere exchange process in E5/M1, since STT is known to be notoriously problematic in past atmospheric chemistry GCMs and transport models.

5 Tropospheric tracers and chemistry

5.1 Carbon monoxide

Tropospheric chemistry is strongly influenced by carbon monoxide (CO). This is mostly due to the reaction of CO with the hydroxyl radical (OH), i.e., CO + OH → CO_2 + H. This reaction establishes a sink of 90–95% for CO (Logan et al., 1981) and of approximately 41% for OH (von Kuhlmann et al., 2003b) in most of the troposphere. Enhanced CO levels generally reduce OH concentrations, influencing the oxidation capacity of the atmosphere.

To evaluate the CO mixing ratios calculated by E5/M1, we compare the model results

to a CO database provided by the National Oceanic and Atmospheric Administration Climate Monitoring and Diagnostic Laboratory (NOAA/CMDL) as presented by Novelli et al. (1998). Only monthly averages are compared here.

As shown in Fig. 13, the measured annual cycle, as well as the magnitude of the CO mixing ratio is well represented by the model for most locations. In many cases the model result agrees very well with the observed values, (e.g., at the location of South Hampton, Bermuda (BMW, Fig. 13), Tenerife, Canary Islands (IZO, Fig. 13) and Mauna Loa, Hawaii (MLO, Fig. 13)). The comparison shows good agreement for the seasonally as well as the overall tendencies over the simulated period. There are also several locations, however, for which the model overestimates CO concentrations (e.g., Wenover, Utah (UTA, Fig. 13). This is mostly an artefact of the coarse model grid, whereby strong gradients near source regions are underestimated, so that these measurements are not representative for the mean CO in the large grid cells of these locations, especially for the sites where the samples are filtered to be representative of background airmasses.

In very remote regions in the southern hemisphere (Palmer station, Antarctica; PSA, Fig. 13) the model seems to overestimate CO mixing ratios. The discrepancies are largest in summer, suggestive of a problem with photochemistry. It might be that OH concentrations in the high latitude southern hemisphere are underestimated, possibly associated with the stratospheric ozone high-bias (Fig. 11), which reduces UV radiation penetration into the troposphere, although it is also conceivable that the CO source strength in the model is too strong.

In Fig. 14 we compare MOPITT satellite data (Deeter et al., 2004) at 700 hPa with model calculated CO for the year 2003. The left panels show the model results post-processed with the MOPITT kernel. The right panels show the relative differences, indicating that the model somewhat overestimates CO over central South America in January and in particular over southern Africa in January and July, which suggests that the biomass burning CO sources in these regions may be overestimated. These results also suggest that especially for Africa the biomass burning emissions early in

the year in the model are partly located too far south. The upper right panel of Fig. 14 nevertheless shows that the model results for January agree quite well with MOPITT, including the southern Ocean near Palmer (light red and blue colours are within the measurement uncertainty).

A more significant issue emerges for simulated CO at high latitudes in the northern hemisphere in July 2003, as shown in the lower right panel of Fig. 14, which suggests that our model underestimates boreal biomass burning emissions. Indeed, the summer of this year was characterised by dryness and strong burning activity in northwestern North America and eastern Siberia. This is confirmed by Fig. 13, which also shows that at high northern latitudes CO was higher than computed in summer, whereas this was not the case for other years. In fact, our model seems to slightly underestimate CO in winter rather than in summer, possibly associated with anthropogenic emissions in East Asia, and the discrepancy in Fig. 14 for 2003 should be considered as a worst case. All in all, Figs. 13 and 14 indicate that CO distributions and seasonalities are simulated quite realistically. The comparison also underscores that in particular the inter-annual variability of biomass burning emissions can be substantial, so that the use of the year 2000 emissions for the entire simulation period can give rise to discrepancies in individual years.

5.2 Reactive Nitrogen: NO_x, HNO_3, and PAN

The key reactive nitrogen compounds important in tropospheric ozone chemistry are NO_x ($NO + NO_2$), HNO_3, and PAN. NO_x is important as a catalyst in the photochemical production cycles for O_3 in the troposphere. HNO_3 and PAN are reaction products and NO_x reservoir species: HNO_3 is highly soluble, and the conversion of NO_x to HNO_3 and subsequent washout or surface deposition represents one of the main losses for reactive nitrogen, while PAN is thermally instable and provides an important source of NO_x to remote regions in subsiding airmasses.

The 5-year mean surface mixing ratios of NO_x and HNO_3 are plotted in Figs. 15 and 16.

The distributions are generally similar to those computed by other models of similar complexity (e.g., van Noije et al., 2006). The surface distributions show the strong weighting of the NO_x and HNO_3 distribution towards the major source regions, especially the northeastern USA, Europe, and eastern Asia; this is particularly pronounced for NO_x, which results from its relatively short lifetime of about a day in the lower troposphere. Secondary maxima are seen in regions of strong biomass burning and biofuel use (South America, central Africa and southern Asia), and the clear influence of oceangoing ship emissions is seen especially in the NO_x distribution over the Atlantic and Indian Oceans between major ports.

An overview of the annual sources and sinks of reactive nitrogen is given in Table 3; the sources are discussed in more detail in Kerkweg et al. (2006b) and Ganzeveld et al. (2006). On the whole, the listed sources are closely balanced by the budgeted sinks; the difference is due to the small stratosphere-troposphere exchange source of about 0.5 Tg(N)/yr. As indicated above, the key loss for reactive nitrogen is via HNO_3, with about half of the total loss being due to wet deposition of HNO_3, and a third of the total due to HNO_3 dry deposition. The loss of aerosol nitrate by sedimentation contributes a further 15–20%, while the direct loss of NO_x due to the dry deposition of NO_2 contributes less than 10% to the total budget.

To evaluate the distributions versus observations, we compare to the compiled observations of Emmons et al. (2000). For NO_x, we have chosen to only compare to NO here, rather than NO+NO_2, due to the much greater difficulty in accurately measuring NO_2 than NO. NO has a strong diurnal variation with a very low mixing ratio at night (due to conversion to NO_2 by reaction with O_3), and nearly all the measurements in the field campaign composites were made during daytime. Thus, we have filtered the model output to use daytime-only values in the comparisons.

The comparisons to selected profiles for NO, HNO_3, and PAN are shown in Fig. 17. The same six regions are shown for each gas, for comparability.

On the whole, E5/M1 reproduces the vertical structure of NO in the observations very well; out of the entire set of 48 profiles, the majority has a form which closely resem-

bles the observations, although there are also several which are considerably different. The profiles have been selected to show examples of both cases. The model has a slight tendency to underestimate the observed mixing ratios in the individual profiles. The overall regression for the 5 years of data (i.e., using each year as an individual data point) is: R^2=0.32 with a slope of 0.58 and an intercept of 7.1 pmol/mol. The correlation is rather good for a comparison of this nature; for comparison, the model MATCH-MPIC, which has been widely used and accepted as applicable for detailed individual field campaign analysis (e.g., Lawrence et al., 2003; Fischer et al., 2006) has a correlation of R^2<0.1 for this same type of comparison to field campaign composites. The tendency of E5/M1 to underestimate the highest mixing ratios in the observations could in part be due to either a deficit of NO_x sources, or to a too rapid conversion to HNO_3 and PAN.

For HNO_3, the model also generally reproduces the shape of the vertical profiles and the variability from region to region, as seen in the selected regional profiles in Fig. 17. Overall, there is a tendency to underestimate the mixing ratios slightly in the lower troposphere, and overestimate in the upper troposphere. The latter may be partly because the model does not yet consider the uptake of HNO_3 on ice (von Kuhlmann and Lawrence, 2006) and the effects of sedimentation of small ice crystals (Lawrence and Crutzen, 1998). The linear regression between all observed and simulated profiles yields R^2=0.39, a slope of 0.59, and an intercept of 57.1 pmol/mol. This is slightly better than the correlation for NO, but the same indications are seen of a tendency to underestimate the highest mixing ratios and the overall variability.

Finally, the comparisons for PAN show a very clear tendency for the model to overestimate the observed mixing ratios (Fig. 17). As for NO and HNO_3, the regression yields a slope of less than one (0.73) and a positive intercept of 190 pmol/mol, indicating an underestimate of the overall variability, though in this case the intercept is large enough that the model statistically overestimates for all mixing ratios up to about 600 pmol/mol. This general tendency to overestimate was also noticed in von Kuhlmann et al. (2003a), in which the MATCH-MPIC model used a very similar chemical scheme for the tropo-

sphere to that used here. von Kuhlmann et al. (2003a) considered possible reasons for this overestimate, including a too low dissociation rate, and sub-grid chemical effects on the formation of PAN, but were not able to resolve the issue entirely; it will still need to be considered further in future studies, where targeted analyses of individual campaigns are more likely to eventually provide insight into this issue.

For HNO_3 and NH_x (NH_3, NH_4^+), wet deposition is the major sink. Summarising the detailed analyses presented in Tost (2006), a comparison of the wet deposition fluxes shows a good agreement of the model results with observations from several measurement networks (e.g. USA, Europe, East Asia). Nevertheless, analysis of the output from the wet deposition scheme (SCAV) indicates that some improvements with respect to the "effective" and "real" liquid water content (LWC) of the falling precipitation are required. The parameterisation is currently being improved, and preliminary results (not shown) indicate a higher, more realistic precipitation LWC. However, this mainly influences the dissolution of weak acids, e.g. HCOOH and CH_3COOH, for which the uptake is now more efficient and a greater fraction is scavenged, while for strong acids, e.g. HNO_3, the uptake was already almost complete at the low LWC, so that the scavenged fraction does not change much.

5.3 Hydroxyl radical

Hydroxyl radical concentrations in the troposphere are computed to be highest in the tropics, as expected. Figure 18 shows its annual distribution at the surface.

Here we see that the highest values are found off the coast of south and south-east Asia and central America, and that ship tracks can be clearly distinguished, coincident with the NO_x distribution in Fig. 15. Over continental regions, especially the tropical forest, surface layer OH concentrations tend to be reduced due to reactions with hydrocarbons. The seasonal zonal averages (Fig. 19) are comparable to the distributions computed by other models (Lawrence et al., 2001), although they show a few important differences to the OH distribution of Spivakovsky et al. (1990). One major difference is that the zonal mean is not symmetric, rather more heavily weighted towards the

northern hemisphere. Another difference is that the maximum OH is located near the surface in the northern hemisphere instead of being centred at about 600 hPa in the tropics as indicated by Spivakovsky et al. (2000). A factor which may contribute to these differences is that the analysis by Spivakovsky et al. (2000) uses monthly means of key species that affect the OH chemistry to compute the OH distribution with a photochemical model. This will tend to misrepresent non-linear effects, such as transitions between different reaction regimes, which are caused by temporal fluctuations of temperature and of other trace gases.

Traditionally one of the most powerful criteria for evaluating global OH is looking at the lifetime of CH_4 and methyl chloroform (Krol et al., 1998; Houghton et al., 2001; Prinn et al., 2001; Spivakovsky et al., 1990, 2000). According to Lawrence et al. (2001), we calculated the tropospheric lifetime of methane as

$$\tau(CH_4) = \frac{\sum M_{CH_4}}{\sum k_{CH_4} \times [OH] \times M_{CH_4}} \quad (1)$$

where k_{CH_4} (taken from Atkinson et al., 2005) and M_{CH_4} are the reaction rate coefficient of CH_4 with OH and the mass of CH_4, respectively. $\sum$ denotes the sum over tropospheric grid boxes. In the last row of Table 4 we see that $\tau(CH_4)$ from our model is lower than from Spivakovsky et al. (2000) and von Kuhlmann (2001).

Other estimates in the literature include a global $\tau(CH_4)$ of 8.67±1.32 based on a recent model inter-comparison by Stevenson et al. (2006). Using the same kinetic data as von Kuhlmann (2001), $\tau(CH_4)$ increases by 2.6% to about 8.3 years consistently with a small decrease of $OH_{GM}(CH_4)$ from 1.32 to 1.31 $\times 10^6$ cm^{-3}. This shows a non-negligible sensitivity to changes in the kinetic parameters, namely the rate constant of the reaction CH_4 + OH. The $\tau(CH_4)$ we calculated is within the variability range of other models (Stevenson et al., 2006).

To obtain an impression of how well our model calculates OH we followed Lawrence et al. (2001) and performed an analysis of the OH field by breaking it down into subdomains using proper weightings that have different dependencies on air mass, air

volume and temperature. We also looked at the annual cycle of OH by sub-domains realizing that the OH concentration always reaches the maximum value in July and in the northern tropics. The reason for this is that the primary formation of OH depends on the amount of UV light and water vapour, and the secondary formation depends on NO_x. Therefore the maximum values occur during summer in the most polluted hemisphere (Fig. 19). In Table 4 the global mean OH concentrations are shown. At first glance it seems that our model performs well globally with differences ranging from 1 to 5% with respect to Spivakovsky et al. (2000). However, this is seen to be a cancellation effect between different regions. In fact from Table 5 we see that compared to von Kuhlmann (2001) the global OH distribution in E5/M1 is quite similar, while compared to Spivakovsky et al. (2000) E5/M1 computes higher OH in the lower troposphere (especially in the tropics where differences are about 30%) and lower OH in the upper troposphere (more evenly distributed over latitudes).

Possible explanations for these differences can be that:

- in the lower troposphere (below 750 hPa) our model setup neglects some important sinks like liquid phase chemistry of OH (though it includes reactions of H_2O_2 and O_3), HO_x uptake by aerosols (for a review of these heterogeneous processes see Jacob, 2000), and secondary organic aerosol (SOA) formation. Some evidence in support of this is that the largest differences are in the tropics where VOC emissions from natural sources and humidity are relatively high;
- in the middle and upper troposphere the lower values compared to Spivakovsky et al. (2000) possibly come from the parameterisation of processes that depend strongly on convection like
  - the vertical transport of HO_x precursors (that could also partly account for the positive differences in the lower troposphere)
  - NO_x production by lightning;
- taking advantage of on-line calculations with short time steps (15 min) our model

may actually be computing a more consistent and thus more realistic distribution than using the approach of Spivakovsky et al. (2000) with a photochemical model that uses monthly means of OH precursors.

5.4 Model comparison with ozone sonde data

To evaluate the model calculated ozone distribution the compilations of balloon sounding data by Logan (1999) and Thompson et al. (2003a,b) have been used (further denoted as Logan and SHADOZ, respectively). The Logan data set offers the advantage of a relatively long time series, hence it can be considered a climatology. It covers the period from 1980 to 1993, while our simulation covers the years 1998 to 2005, so that anomalies such as El Niño events and trends may impede the model-data comparison. The SHADOZ measurements, on the other hand, coincide with our model simulation period although the data set is smaller and less useful for statistical analyses. The SHADOZ measurements furthermore involve stations primarily in the tropics and the southern hemisphere whereas the Logan data are more widespread so that the data sets are complementary. From the SHADOZ data we derived a climatological average (1998–2002) for each location, similar to the Logan compilation.

5.4.1 Vertical profiles

While the model comparison with TOMS satellite data indicates a slight positive model bias in the column ozone at middle to high latitudes, as discussed in Sect. 4 (Fig. 11), the analysis for the troposphere based on the Logan data gives no evidence of systematic positive or negative biases (Fig. 20).

Over Japan (Kagoshima) in winter the model seems to significantly overestimate ozone in the free troposphere and tropopause region, most likely related to relatively strong downward transport from the stratosphere, whereas in summer the model calculated ozone in the lower free troposphere in this location is relatively low. In addition, upper tropospheric ozone over Lauder in the model seems relatively high, i.e., near the

upper bound of the measurement uncertainty range, which is consistent with the bias in total ozone (cf. Fig. 11). In general, the modeled ozone profiles match within one sigma standard deviation of the measurements. Figure 20 also shows that the model calculated variability is typically highest in the upper troposphere, related to the influence of synoptic weather systems on stratosphere-troposphere exchange, in agreement with the measurement data.

5.4.2 Annual time series

The seasonal cycles of ozone in the middle troposphere of the Logan and SHADOZ data along with our model results are shown in Figs. 21 and 22, respectively.

We focus on 400 hPa because Fig. 20 indicates that model deviations at this level may be most significant. The comparison between the ozone time series in Fig. 21 indicates that the model generally reproduces the observed seasonal dependencies, i.e., well within the standard deviations of both data sets, and the ozone variability in both model and measurement data are very similar. Again, over Japan (Kagoshima) our model seems to overestimate ozone concentrations in winter, likely related to too strong transport from the stratosphere. Over Alert, the model overestimates ozone in late winter, possibly for the same reason, although the local tropopause concentrations fit the data well (Fig. 20), thus indicating that long-distance transport to high northern latitudes might be too strong. Also at Lauder the model seems to be high-biased, although Fig. 20 shows that the agreement improves both at lower and higher altitudes.

Over Hohenpeissenberg our model underestimates free tropospheric ozone in summer, possibly related to a deficiency in the convective transport of precursor gases. An alternative explanation is that the Logan data base covers the period 1980–1993, during which the summertime ozone concentrations peaked, whereas during subsequent years the ozone levels have decreased at this location. The model-data comparison for the tropical stations in Fig. 22 generally shows good agreement, although the sparseness of the data set precludes a detailed model evaluation. Nevertheless, middle tropospheric ozone over Paramaribo ("Param") is clearly too low from June to

October. We explain this by a model bias in biomass burning emissions and transport from Brazil in the dry season.

The Taylor diagram in Fig. 23 summarises the comparison of all sonde data at 400 hPa from the Logan climatology.

The model-data correlation is high, mostly above 0.6, suggesting that the seasonal dependency of model calculated ozone is quite realistic. The clustering of the data points around a normalised standard deviation of one furthermore corroborates the absence of systematic model biases. A Taylor diagram for the model comparison with the SHADOZ tropospheric ozone data, averaged to the same pressure levels as in the Logan climatology, is shown in Fig. 24. In spite of several outliers, the points cluster around a normalised standard deviation of one and a correlation coefficient above 0.8, thus confirming the good agreement.

6 Stratospheric tracers and chemistry

6.1 Model comparison with MIPAS data

In this section we compare model calculated O_3 and HNO_3 with the MIPAS satellite data averaged over the years 2002 and 2003 (Glatthor et al., 2005a; Mengistu Tsidu et al., 2005). Nitric acid is included as an example of a reservoir species of ozone destroying gases, being controlled both by transport and chemistry. The northern winter (DJF) and the Antarctic spring season (SON) are shown in Figs. 25 and 26.

The model results are typically within the observational error range of about 5% (O_3 above about 100 hPa) and 10% (HNO_3) although the difference graphs in the right panels indicate some deviations. The simulated ozone agrees rather well with the observations, although there are two regions with typical difference patterns. The threefold difference structure in the tropical stratosphere points to the sensitivity of ozone to the correct representation of the QBO, in particular because the results improve in the S2 simulation with reduced nudging and gravity wave forcing, in which the QBO phase

shift is diminished as compared to S1. The higher ozone in the model near the peak at 10 hPa is mostly related to the coarser vertical resolution of the MIPAS data, as indicated by test calculations with model data convolved with the MIPAS averaging kernels (not shown).

In polar latitudes the model tends to underestimate ozone depletion in the lowermost stratosphere, especially in the Arctic winter. Because the downward transport is too weak, insufficient chlorine and bromine are available, resulting in too little ozone destruction by heterogeneous chemistry on PSCs. In the Antarctic spring the ozone hole below about 30 hPa is well represented though somewhat underestimated below 70 hPa. The overestimation of ozone around 7 hPa during SON in the Antarctic is a consequence of the lack of NO_y from downward transport from the thermosphere (Funke et al., 2005a) in the model.

Also for HNO_3 (Fig. 26) the model reproduces the observed distribution quite well, including the denitrified regions in the Antarctic ozone hole region. The maximum of HNO_3 is almost perfectly captured by the model. The slight underestimation of HNO_3 throughout the lower stratosphere by the model is attributed to the missing reaction $NO + HO_2 \rightarrow HNO_3$ (Butkovskaya et al., 2005). The dipolar difference pattern in DJF in the Arctic is again due to the too weak downward motion, whereas the missing HNO_3 during SON in the middle and upper stratosphere is related to the solar proton event and enhanced transport of nitrogen oxides from the thermosphere (Stiller et al., 2005; López-Puertas et al., 2005a,b). In the Antarctic the effect of the missing source propagates downward near the vortex edge, the region with the largest downward motion. A more detailed comparison between the model and MIPAS data, including additional reactive nitrogen and chlorine species, will be presented in a follow-up paper with a focus on the stratospheric part of the model domain.

6.2 Model comparison with sonde data

6.2.1 Vertical profiles

In Fig. 27 we compare the model results with selected sounding stations from the Logan climatology, being representative of different latitudes.

The agreement is rather good for most locations, both in terms of concentrations and variability. The largest discrepancies are found for the middle stratosphere at high latitudes (Alert, Resolute) where the model tends to overestimate ozone. This might partly be associated with a time-mismatch and the large interannual variability at this location. At the other locations the agreement is somewhat poorer especially around 40 hPa, indicating that the model slightly overestimates ozone, although the results are generally within the standard deviations. The good model agreement with tropical measurement data is confirmed by the comparison with the SHADOZ profiles in Fig. 28.

The stratospheric vertical ozone maxima from the Logan climatology have been collocated with the model results in Fig. 29, showing a very high correlation coefficient ($R^2 \approx 0.9$), and confirming a slight positive bias in the extra-tropics.

Note that this bias substantially decreases in our S2 simulation with reduced nudging in the lowermost stratosphere and weaker gravity wave forcing.

6.2.2 Annual time series

In the model results for the extra-tropical stratosphere some deviations with measurement data are found for the region around 40 hPa. The monthly variation of ozone at this level is compared with selected sonde station data from the Logan climatology in Fig. 30.

The seasonal dependence as well as the variability is very well captured by the model, although a small positive bias up to about 0.5 µmol/mol is apparent for several locations. We speculate that some of the discrepancy might be related to a slight over-prediction of molecular oxygen photodissociation in the stratosphere. The model-

data discrepancy seems to be largest at middle latitudes and in winter, associated with relatively rapid transport in the Brewer-Dobson circulation. The overall high correlation between model results and observations, generally above 0.8, is confirmed by the Taylor diagram in Fig. 31.

The clustering around the normalised standard deviation of one supports the impression of good agreement. The few outliers, e.g. in the tropics, represent sparse components of the data set and should not be overrated. This overall positive picture is reinforced by the comparison with the tropical SHADOZ data in Fig. 32, for which we derive a correlation coefficient of R=0.8.

To further improve the model results in the future, we intend to use the S2 setup of the model, though we stress that more research will be needed to optimise the gravity wave forcing in the model.

7 Summary and conclusions

We have introduced the new MESSy model, which includes a comprehensive modular description of atmospheric chemistry processes, being straightforward to implement in atmospheric transport and general circulation models through its standardised interface. It can easily be extended with new modules, either to improve and test existing ones or to further develop the system into an Earth system model. Model setups can be changed by selecting modules and parameter settings in the namelists of the computer programme, which implies that different setups can be used in sensitivity studies with the same executable, i.e. under identical numerical conditions.

In the present work MESSy has been coupled to the ECHAM5 general circulation model, to be used both to predict and analyse actual atmospheric chemical conditions, or as a chemistry-climate model. In the latter case long-term integrations may require concessions with respect to the level of complexity applied in view of computational costs.

We presented an application in which a simple data assimilation method, i.e. by

nudging towards ECMWF meteorological data by Newtonian relaxation, has been employed to simulate realistic synoptic conditions, allowing a direct comparison of model output with measurement data. The relaxation coefficients have been chosen to be as small as feasible, and this weak nudging was limited to the tropospheric part of the model domain to allow maximum internal and numerical consistency in the computation of meteorological processes. The tropospheric wave forcing of the stratospheric circulation has been simulated successfully, as shown by the simulation of the QBO and a major Antarctic stratospheric warming event.

By simulating the period of 1998–2005 it was possible to compare with long-term climatological atmospheric chemistry data from measurement networks and satellites. The MESSy modules and the 8-year output are available on request through the internet address http://www.messy-interface.org, which also provides a user-friendly web-based graphics tool to select data for geographical regions and time periods, and to download or plot the data in different coordinates. We hope that colleagues will use the model results, compare them with measurement data and report possible virtues and shortcomings. It must be emphasised, though, that the model was applied at T42 resolution and 90 layers up to 0.01 hPa, being most suited for simulations of the stratosphere and the tropopause region. For detailed comparisons with measurements in the troposphere a higher resolution may be desirable. For example, for a model setup with a focus on the troposphere a higher horizontal and vertical resolution can be selected, and the computation of stratospheric processes can be scaled down by using the results presented here to constrain the model above the tropopause. The present resolution has been chosen as a compromise between model accuracy and CPU time efficacy.

Our model evaluation included a comparison with selected physical parameters to test if the coupling of chemistry modules to ECHAM5 affects the simulation of meteorological processes, with a focus on key parameters influencing atmospheric chemistry such as temperature and moisture. It appears that the model simulates the water vapour column and geographical distribution very realistically, apart from a significant

overestimation in the subtropical southern hemisphere during winter. Precipitation patterns are simulated realistically, too, although in the SPCZ and ITCZ regions, especially at about 15°S, and along the Andes mountains and in northwestern Tibet in summer convective rainfall appears to be overestimated.

Simulated temperature distributions in the stratosphere, both statistically and synoptically, have been compared to MIPAS satellite data, and the model results largely agree within the observational uncertainty of about 2 K. Cold biases in the wintertime lower polar stratosphere, notorious in many models, including our previous model version, have diminished. At higher altitudes (≈25 hPa) in the southern hemisphere during winter the model still has a slight warm bias at middle latitudes and a cold bias of a few K at high latitudes, associated with too weak subsidence within the Antarctic vortex, being confirmed by comparisons of simulated tracer distributions with satellite data (O_3, N_2O).

Sensitivity simulations (S2) with a reduced gravity wave forcing (by 10%) and a reduced nudging near the tropopause (to ≈200 hPa instead of ≈100 hPa) indicate even closer agreement with observations. The modelled zonal wind reversals in the tropics by the QBO agree well with meteorological observations, especially in the S2 setup of the model, and it can be concluded that in particular the tropical branch of the Brewer-Dobson circulation is represented highly accurately. Detailed comparisons between satellite data and the model results for the Antarctic spring of 2002 show that the model closely reproduces the major stratospheric warming event that caused the extraordinary vortex split in September of that year. Again the results were most accurate in the S2 version of the model, i.e. in which the model was left the largest degree of freedom in simulating the middle atmosphere.

Our model analysis of tropospheric tracers focused on CO and reactive nitrogen compounds, being central in the photochemistry of global ozone and oxidation processes. Although hydrocarbons are also important in this respect, the multitude of species and reactions involved will be done justice by presenting the results in a sep-

arate publication (Pozzer et al., 2006[2]). The comparison of simulated CO with in situ measurements at ground-based background stations shows good agreement, although steep concentration gradients near polluted areas are difficult to capture with the T42 resolution. The comparison of model results with MOPITT satellite CO data suggests that global and regional CO distributions are well captured, while the simulated biomass burning CO source in Africa may be somewhat too strong. The model underestimates CO emissions from boreal fires in the summer of 2003, though not in other years, which shows that it would be desirable to more realistically represent the inter-annual variability of biomass burning emissions.

The model results for reactive nitrogen species have been evaluated with a focus on NO, HNO_3 and PAN. The model accurately reproduces the characteristic C-shaped altitude profiles of NO in polluted regions as well as the low boundary layer mixing ratios typical for the remote oceans. The model also captures HNO_3 profiles as measured by aircraft, although in several cases upper tropospheric mixing ratios are overestimated, probably because HNO_3 removal through the sedimentation of ice particles is neglected. PAN mixing ratios are systematically overestimated, possibly related to the parameterisation of chemical reactions between nitrogen oxides and organic compounds, although the shape of the altitude distribution seems well captured.

Global OH distributions have been tested by comparing with other models and by contrasting the lifetimes of long-lived tracers such as methyl chloroform and methane with empirical data. Although the tracer lifetimes are quite comparable with earlier estimates, we find that especially the computed vertical OH distributions can differ substantially compared to earlier work. We assume that the advancements in our model with respect to the consistency and comprehensiveness of convection, emissions (e.g. NO_x from lightning), multiphase chemistry and deposition processes have improved the simulations of global OH. However, the ultimate test is still pending, and

[2] Pozzer, A., Jöckel, P., Sander, R., Ganzeveld, L., Kerkweg, A., and Lelieveld, J.: Simulating organic species with the global chemistry-climate model ECHAM5/MESSy: a comparison of model results and observations, Atmos. Chem. Phys. Discuss., in preparation, 2006a.

we will need to substantiate this through more detailed analyses of individual measurement campaigns.

The computed profiles and distributions of ozone in the troposphere and stratosphere have been tested by comparing with climatological data sets from O_3 soundings and satellite observations. In general, the simulated mean ozone distribution and variability seem to be captured very well by the model. In the middle and upper extra-tropical stratosphere the poleward transport might be slightly too rapid, giving rise to a small high-bias in ozone, although the model-data comparison further improves in the S2 sensitivity simulation. In the polar lower stratosphere ozone destruction by reactive chlorine and bromine species is slightly underestimated, associated with too weak subsidence and delayed downward transport of these species within the vortex. The model accurately reproduces the observed HNO_3 distribution, including the effect of denitrification by sedimenting PSC particles over the poles.

We conclude that our global chemistry-GCM, ECHAM5/MESSy1, consistently simulates the photochemical and dynamical processes that determine ozone in the lower and middle atmosphere up to 0.01 hPa. To our knowledge this is the first time that a free running model, albeit with weak nudging towards ECMWF meteorological analyses in the troposphere, reproduces the steep ozone gradients across the tropopause, both in the tropics and extra-tropics, without prescribed boundary conditions. This is a strong indication that stratosphere-troposphere coupling processes are simulated accurately, even though over some regions, notably over Japan in winter, the downward flux of O_3 may be too strong. We expect, though, that this will improve at higher resolutions. Our results corroborate the importance of the QBO in simulating vertical ozone distributions in the stratosphere. Especially in the S2 simulation the comparison with satellite observations is very good, indicating that this model setup is particularly well-suited to simulate stratospheric processes and stratosphere – troposphere interactions.

Appendix A

The following modifications and additions have been applied to ECHAM5:

- The nudging routines have been fully vectorised and parallelised to allow the application of the nudging technique without further restrictions w.r.t. the technical setup of the model. Nudging can now be applied in any ECHAM5 supported domain decomposition (parallelisation) and vector length (vectorisation) combination.
- The calculation of the initial values in the vertical diffusion scheme have been modified, to be consistent with the applied leapfrog time integration scheme and filter (Asselin, 1972).
- Convection, cloud, and radiation subroutines have been replaced by the MESSy submodels CONVECT, CLOUD, and RAD4ALL, respectively. In the present study, the MESSy submodels give identical results to the original ECHAM5 routines. The recoding serves the straightforward implementation of alternative process descriptions, including the option to test the submodels under identical numerical conditions by using the same executable (e.g., CONVECT, Tost, 2006; Tost et al., 2006[3]), and/or the implementation of additional couplings between processes (e.g., radiation-aerosol, cloud-aerosol) in the future.
- The convective tracer transport of ECHAM5 has been modified to guarantee positive definite results (Brinkop and Sausen, 1996). Note that for the present study the convective tracer transport has been calculated with the submodel CVTRANS, which is a convection-scheme independent implementation.
- The ECHAM5 output routines have been expanded to allow the output of time average and standard deviation, as an alternative to the output of instantaneous

[3]Tost, H., Jöckel, P., and Lelieveld, J.: Influence of different convection parameterisations in a GCM, Atmos. Chem. Phys. Discuss., in preparation, 2006b.

fields. Furthermore, the data representations SCALAR, COLUMN, and ARRAY1D have been added.

– The build process (configure/gmake) for user-friendly compilation of the source code has been completely revised.

Appendix B

The following submodels are also part of MESSy version 1.1, but have not been used in this study:

AIRSEA (Pozzer et al., 2006b[4]) calculates the exchange of chemical tracers between the ocean and atmosphere using a two-layer approach. The submodel simulates in particular the bi-directional transport of volatile organic compounds and their oxidation products. The successful use of this submodel is dependent on the availability of observations of the distribution of organic tracers in seawater.

EMDEP (Ganzeveld et al., 2006) combines the calculations of online emissions (VOC, NO, DMS, sea-salt, dust, and organic and black carbon), and the dry deposition of gases and aerosols following the "big-leaf"-approach. It is the developer implementation of the emission and deposition routines, and formed the basis for the submodels ONLEM and DRYDEP.

M7 (Vignati et al., 2004; Stier et al., 2005) is an aerosol dynamics model that redistributes the particle numbers and masses between 7 modes and from the gas to the aerosol phase (for each mode), by nucleation, condensation and coagulation.

MECCA_MBL is a sub-submodel of MECCA for calculating the aerosol chemistry in the marine boundary layer.

[4]Pozzer, A., Jöckel, P., Sander, R., Ganzeveld, L., and Lelieveld, J.: Technical Note: The MESSy-submodel AIRSEA calculating the air-sea exchange of chemical species, Atmos. Chem. Phys. Discuss., submitted, 2006b.

PHOTO is the developer implementation of the fast online photolysis rate calculation scheme which formed the basis for JVAL. It is closer to the original code of Landgraf and Crutzen (1998), but less general than JVAL.

Appendix C

Following are the statistical methods employed in this study: m_i is the simulated (model), and o_i the observed value. The relative errors are δ_i^m and δ_i^o, respectively. The model "error" is the variability calculated from the averaged output values, and the measurement error is a combination of instrumental errors and variance. The difference is defined as:

$$d_i = m_i - o_i \ , \ d_i = f(o_i, m_i) \tag{C1}$$

Any classical statistical calculation can be weighted using $1/\epsilon_i$ as a weighting factor, where

$$\epsilon_i = \sqrt{\delta_i^{m2} + \delta_i^{o2}} \tag{C2}$$

This allows an independent statistical analysis, whereby each value is scaled with the geometrical average of the errors. We use the following statistical functions (C2):

– standard deviations:

$$\sigma_m = \left[\frac{1}{N} \sum_{i=1}^{N} \left(\frac{m_i - \overline{m}}{\epsilon_i} \right)^2 \right]^{1/2} \tag{C3}$$

$$\sigma_o = \left[\frac{1}{N} \sum_{i=1}^{N} \left(\frac{o_i - \overline{o}}{\epsilon_i} \right)^2 \right]^{1/2} \tag{C4}$$

– Root Mean Square (RMS)

$$E = \left[\frac{1}{N}\sum_{i=1}^{N}\left(\frac{m_i - o_i}{\epsilon_i}\right)^2\right]^{1/2} = \left[\frac{1}{N}\sum_{i=1}^{N}\left(\frac{d_i}{\epsilon_i}\right)^2\right]^{1/2} \quad \text{(C5)}$$

– Correlation coefficient

$$R = \frac{\frac{1}{N}\sum_{i=1}^{N}\left(\frac{(m_i-\overline{m})(o_i-\overline{o})}{\epsilon_i^2}\right)}{\sigma_m \sigma_o} \quad \text{(C6)}$$

– Centred pattern RMS difference

$$E' = \left[\frac{1}{N}\sum_{i=1}^{N}\left[\left(\frac{m_i - \overline{m}}{\epsilon_i}\right) - \left(\frac{o_i - \overline{o}}{\epsilon_i}\right)\right]^2\right]^{1/2} \quad \text{(C7)}$$

To apply this approach to the Taylor diagrams (Taylor, 2001), the basic relationship between the variables E', σ_m, σ_o and R must hold:

$$E'^2 = \sigma_m^2 + \sigma_o^2 - 2\sigma_m\sigma_o R \quad \text{(C8)}$$

Using the definitions C3 to C6 yields:

$$\frac{1}{N}\left[\sum_{i=1}^{N}\left(\frac{m_i - \overline{m}}{\epsilon_i}\right)^2 + \sum_{i=1}^{N}\left(\frac{o_i - \overline{o}}{\epsilon_i}\right)^2 - 2\sum_{i=1}^{N}\left(\frac{m_i - \overline{m}}{\epsilon_i}\right)\left(\frac{o_i - \overline{o}}{\epsilon_i}\right)\right] = \frac{1}{N}\left[\sum_{i=1}^{N}\left[\left(\frac{m_i - \overline{m}}{\epsilon_i}\right) - \left(\frac{o_i - \overline{o}}{\epsilon_i}\right)\right]^2\right] . \quad \text{(C9)}$$

Hence (from C9):

$$\frac{1}{N}\sum_{i=1}^{N}\left(\frac{d_i-\overline{d}}{\epsilon_i}\right)^2 = E'^2 \text{ as in Eq. C7} \tag{C10}$$

This approach can be applied in different types of data analysis, like time-series or vertical profile analysis.

The average and RMS are dimensionless (normalised to ϵ_i). To obtain a non-normalised value the statistic functions have to be multiplied by the average of the weighting factor:

$$\widehat{\overline{\epsilon}} = \left[\frac{1}{N}\sum_{i=1}^{N}{\epsilon_i}^2\right]^{1/2} = \left[\frac{1}{N}\sum_{i=1}^{N}(\delta_i^{m2}+\delta_i^{o2})\right]^{1/2} \tag{C11}$$

Acknowledgements. The authors wish to thank E. Roeckner and the model development team at the MPI for Meteorology for the ECHAM5 development, M. Giorgetta (MPI for Meteorology) for the 90-layer version and helpful suggestions, E. Manzini (INGV, Bologna) for helpful suggestions on the gravity wave parameterisation, C. Kurz, A. Lauer, V. Grewe, M. Dameris, R. Sausen (DLR Oberpfaffenhofen) for useful discussions, H. Lederer and his team (Max-Planck Computer Centre in Garching near Munich) for their support, P. Zimmermann and T. Butler for help with creating the emission dataset, the EU (Project SCOUT-O3) and the BMBF (Projects KLIMEX, HGF-ENVISAT) for funding, the International Max Planck Research School for Atmospheric Chemistry and Physics for support, D. Stevenson (School of Geosciences, University of Edinburgh) for providing the results from the model inter-comparison project. The authors further wish to acknowledge the use of the Ferret program for analysis and graphics in this paper. Ferret is a product of NOAA's Pacific Marine Environmental Laboratory (information is available at http://ferret.pmel.noaa.gov/Ferret/).

References

Adler, R. F., Kidd, C., Petty, G., Morissey, M., and Goodman, H. M.: Intercomparison of global precipitation products: The third Precipitation Intercomparison Project (PIP-3), Bul. Am. Meteorol. Soc., 82, 1377–1396, 2001. 6969

Asselin, R.: Frequency filter for time integrations, Mon. Weather Rev., 100, 487–490, 1972. 6998

Atkinson, R., Baulch, D. L., Cox, R. A., Crowley, J. N., Hampson Jr., R. F., Hynes, R. G., Jenkin, M. E., Kerr, J. A., Rossi, M. J., and Troe, J.: Summary of evaluated kinetic and photochemical data for atmospheric chemistry: Web version March 2005, http://www.iupac-kinetic.ch.cam.ac.uk/, 2005. 6986

Austin, J., Shindell, D., Beagley, S. R., Brühl, C., Dameris, M., Manzini, E., Nagashima, T., Newman, P., Pawson, S., Pitari, G., Rozanov, E., Schnadt, C., and Shepherd, T. G.: Uncertainties and assessments of chemistry-climate models of the stratosphere, Atmos. Chem. Phys., 3, 1–27, 2003. 6959, 6973

Bengtsson, L., Hodges, K. I., and Hagemann, S.: Sensitivity of large-scale atmospheric analysis to humidity observations and its impact on the global water cycle and tropical and extratropical weather systems in ERA40, Tellus, 56A, 202–217, 2004. 6972

Brinkop, S. and Sausen, R.: A modified mass-flux scheme for convection which maintains positive tracer concentrations, Tech. Rep. 67, Institut für Physik der Atmosphäre DLR, 1996. 6961, 6998

Brühl, C. and Crutzen, P. J.: NO_x-catalyzed ozone destruction and NO_x activation at midlatitudes to high latitudes as a main cause of the spring to fall ozone decline in the Northern Hemisphere, J. Geophys. Res., 105, 12 163–12 168, 2000. 6979

Buchholz, J.: Simulations of physics and chemistry of polar stratospheric clouds with a general circulation model, Ph.D. thesis, University of Mainz, Germany, http://nbn-resolving.de/urn/resolver.pl?urn=urn:nbn:de:hebis:77-8187, 2005. 6964

Butkovskaya, N. I., Kukui, A., Pouvesle, N., and Le Bras, G.: Formation of nitric acid in the gas-phase HO2 + NO reaction: Effects of temperature and water vapor, J. Phys. Chem. A, 109, 6509–6520, 2005. 6991

Crutzen, P. J. and Brühl, C.: Catalysis by NO_x as the main cause of the spring to fall stratospheric ozone decline in the Northern Hemisphere, J. Phys. Chem., 105-A, 1579–1582, 2001. 6979

Deeter, M. N., Emmons, L. K., Francis, G. L., Edwards, D. P., Gille, J. C., Warner, J. X., Khattatov, B., Ziskin, D., Lamarque, J.-F., Ho, S. P., Yudin, V., Attie, J.-L., Packman, D., Chen, J., Mao, D., Drummond, J. R., Novelli, P., and Sachse, G.: Evaluation of operational radiances for the Measurements of Pollution in The Troposphere (MOPITT) instrument CO thermal band channels, J. Geophys. Res., 109, D03308, doi:10.1029/2003JD003970, 2004. 6981

Emmons, L. K., Hauglustaine, D. A., Müller, J.-F., Carroll, M. A., Brasseur, G. P., Brunner, D., Staehelin, J., Thouret, V., and Marenco, A.: Data composites of airborne observation of tropospheric ozone and its precursor, J. Geophys. Res., 105, 20 497–20 538, 2000. 6983, 7035

Endemann, M., Garé, P., Langen, J., Nett, H., and Readings, C. J.: MIPAS – An Envisat Instrument for Atmospheric Chemistry and Climate Research, Tech. rep., ESA, ESA bulletin 101, http://www.esa.int/esapub/bulletin/bullet101_.htm, 2000. 6975

Fischer, H., Lawrence, M. G., Gurk, C., Hoor, P., Lelieveld, J., Hegglin, M. I., Brunner, D., and Schiller, C.: Model simulations and aircraft measurements of vertical, seasonal, and latitudinal O_3 and CO distributions over Europe, Atmos. Chem. Phys., 6, 339–348, 2006. 6984

Funke, B., López-Puertas, M., Gil-López, S., von Clarmann, T., Stiller, G. P., Fischer, H., and Kellmann, S.: Downward transport of upper atmospheric NO_x into the polar stratosphere and lower mesosphere during the Antarctic 2003 and Arctic 2002/2003 winters, J. Geophys. Res., 110, D24308, doi:10.1029/2005JD006463, 2005a. 6991

Funke, B., López-Puertas, M., von Clarmann, T., Stiller, G. P., Fischer, H., Glatthor, N., Grabowski, U., Höpfner, M., Kellmann, S., Kiefer, M., Linden, A., Mengistu Tsidu, G., Milz, M., Steck, T., and Wang, D. Y.: Retrieval of stratospheric NO_x from 5.3 and 6.2 μm nonlocal thermodynamic equilibrium emissions measured by Michelson Interferometer for Passive Atmospheric Sounding (MIPAS) on Envisat, J. Geophys. Res., 110, D09302, doi:10.1029/2004JD005225, 2005b. 6976

Ganzeveld, L. N., van Aardenne, J., Butler, T., Lawrence, M. G., Metzger, S. M., Stier, P., Zimmerman, P., and Lelieveld, J.: Technical Note: Anthropogenic and natural offline emissions and the online EMissions and dry DEPosition (EMDEP) submodel of the Modular Earth Submodel System (MESSy), Atmos. Chem. Phys. Discuss., 6, 5457–5483, 2006. 6960, 6964, 6983, 6999

Giorgetta, M. A. and Bengtsson, L.: The potential role of the quasi-biennial oscillation in the stratosphere-troposphere exchange as found in water vapour in general circulation model

experiments, J. Geophys. Res., 104, 6003–6019, 1999. 6965
Giorgetta, M. A., Manzini, E., and Roeckner, E.: Forcing of the quasi-biennial oscillation from a broad spectrum of atmospheric waves, Geophys. Res. Lett., 29, 1245, doi:10.1029/2002GL014756, 2002. 6967
Giorgetta, M. A., Manzini, E., Roeckner, E., Esch, M., and Bengtsson, L.: Climatology and forcing of the quasi-biennial oscillation in the MAECHAM5 model, J. Climate, in press, 2006. 6967, 6968
Glatthor, N., von Clarmann, T., Fischer, H., Funke, B., Grabowski, U., Höpfner, M., Kellmann, S., Kiefer, M., Linden, A., Milz, M., Steck, T., Stiller, G. P., Mengistu Tsidu, G., and Wang, D. Y.: Mixing processes during the Antarctic vortex split in September/October 2002 as inferred from source gas and ozone distributions from ENVISAT-MIPAS, J. Atmos. Sci., 62, 787–800, 2005. 6974
Glatthor, N., von Clarmann, T., Fischer, H., Funke, B., Gil-López, S., Grabowski, U., Höpfner, M., Kellmann, S., Linden, A., López-Puertas, M., Mengistu Tsidu, G., Milz, M., Steck, T., Stiller, G. P., and Wang, D. Y.: Retrieval of stratospheric ozone profiles from MIPAS/ENVISAT limb emission spectra: A sensitivity study, Atmos. Chem. Phys., 6, 2767–2781, 2006. 6976, 6990
Grewe, V., Brunner, D., Dameris, M., Grenfell, J. L., Hein, R., Shindell, D., and Staehelin, J.: Origin and variability of upper tropospheric nitrogen oxides and ozone at northern mid-latitudes, Atmos. Environ., 35, 3421–3433, 2001. 6963
Hagemann, S., Arpe, K., and Roeckner, E.: Evaluation of the hydrological cycle in the ECHAM5 model, J. Climate, in press, 2006. 6961, 6968, 6969, 6972
Hines, C. O.: Doppler spread parameterization of gravity wave momentum deposition in the middle atmosphere. Part I: Basic formulation, J. Atmos. Solar. Terr. Phys., 59, 371–386, 1997a. 6968
Hines, C. O.: Doppler spread parameterization of gravity wave momentum deposition in the middle atmosphere. Part II: Broad and quasi monochromatic spectra and implementation, J. Atmos. Solar. Terr. Phys., 59, 387–400, 1997b. 6968
Houghton, J. T., Ding, Y., Griggs, D. J., Nouger, M., van der Linden, P. J., Dai, X., Maskell, K., and Johnson, C. A.: IPCC – Climate Change 2001: The Scientific Basis. Contribution of Working Group I to the third Assessment Report of the Intergovernmental Panel on Climate Change, Cambridge University Press, 2001. 6986
Huffman, G. J., Adler, R. F., Arkin, P., Chang, A., Ferraro, R., Gruber, A., Janowiak, J., McNab,

A., Rudolf, B., and Schneider, U.: The Global Precipitation Climatology Project (GPCP) combined precipitation dataset, Bul. Am. Met. Soc., 78, 5–20, 1997. 6969

Jacob, D. J.: Heterogeneous chemistry and tropospheric ozone, Atmos. Environ., 34, 2131–2159, 2000. 6987

Jeuken, A. B. M., Siegmund, P. C., Heijboer, L. C., Feichter, J., and Bengtsson, L.: On the potential of assimilating meteorological analyses in a global climate model for the purpose of model validation, J. Geophys. Res., 101, 16 939–16 950, 1996. 6968

Jöckel, P.: Technical Note: Recursive rediscretisation of geo-scientific data in multiple dimensions in the Modular Earth Submodel System (MESSy) data import interface, Atmos. Chem. Phys. Discuss., 6, 4673–4688, 2006. 6964

Jöckel, P., Sander, R., Kerkweg, A., Tost, H., and Lelieveld, J.: Technical Note: The Modular Earth Submodel System (MESSy) - a new approach towards Earth System Modeling, Atmos. Chem. Phys., 5, 433–444, 2005. 6959, 6961

Kerkweg, A.: Global Modelling of Atmospheric Halogen Chemistry in the Marine Boundary Layer, Ph.D. thesis, University of Bonn, Germany, http://hss.ulb.uni-bonn.de/diss_online/math_nat_fak/2005/kerkweg_astrid/, 2005. 6962

Kerkweg, A., Buchholz, J., Ganzeveld, L., Pozzer, A., Tost, H., and Jöckel, P.: Technical Note: An implementation of the dry removal processes DRY DEPosition and SEDImentation in the Modular Earth Submodel System (MESSy), Atmos. Chem. Phys. Discuss., 6, 6853–6901, 2006a. 6962, 6965

Kerkweg, A., Sander, R., Tost, H., and Jöckel, P.: Technical Note: Implementation of prescribed (OFFLEM), calculated (ONLEM), and pseudo-emissions (TNUDGE) of chemical species in the Modular Earth Submodel System (MESSy), Atmos. Chem. Phys. Discuss., 6, 5485–5504, 2006b. 6963, 6964, 6966, 6983

Krol, M., van Leeuwen, P. J., and Lelieveld, J.: Global OH trend inferred from methylchloroform measurements, J. Geophys. Res., 103, 10 697–10 711, 1998. 6986

Landgraf, J. and Crutzen, P. J.: An efficient method for online calculations of photolysis and heating rates, J. Atm. Sci., 55, 863–878, 1998. 6962, 7000

Lang, R. and Lawrence, M. G.: Improvement of the vertical humidity distribution in the chemistry-transport model MATCH through increased evaporation of convective precipitation, Geophys. Res. Lett., 32, L17812, doi:10.1029/2005GL023172, 2005a. 6969

Lang, R. and Lawrence, M. G.: Evaluation of the hydrological cycle of MATCH driven by NCEP reanalysis data: Comparison with GOME water vapor field measurements, Atmos. Chem.

Phys., 5, 887–908, 2005b. 6969, 6971
Lawrence, M. G. and Crutzen, P. J.: The impact of cloud particle gravitational settling on soluble trace gas distributions, Tellus, 50B, 263–289, 1998. 6984
Lawrence, M. G. and Rasch, P. J.: Tracer transport in deep convective updrafts: plume ensemble versus bulk formulations, J. Atm. Sci., 62, 2880–2894, 2005. 6962
Lawrence, M. G., Jöckel, P., and von Kuhlmann, R.: What does the global mean OH concentration tell us?, Atmos. Chem. Phys., 1, 37–49, 2001. 6985, 6986
Lawrence, M. G., Rasch, P. J., von Kuhlmann, R., Williams, J., Fischer, H., de Reus, M., Lelieveld, J., Crutzen, P. J., Schultz, M., Stier, P., Huntrieser, H., Heland, J., Stohl, A., Forster, C., Elbern, H., Jakobs, H., and Dickerson, R. R.: Global chemical weather forecasts for field campaign planning: predictions and observations of large-scale features during MINOS, CONTRACE, and INDOEX, Atmos. Chem. Phys., 3, 267–289, 2003. 6984
Logan, J. A.: An analysis of ozone-sonde data for the troposphere: Recommendations for testing 3-D models and development of a gridded climatology for tropospheric ozone, J. Geophys. Res., 104, 16 115–16 149, 1999. 6988, 7038, 7039, 7041, 7045, 7047, 7048, 7049
Logan, J. A., Prather, M. J., Wofsy, S. C., and McElroy, M. B.: Tropospheric chemistry: A global perspective, J. Geophys. Res., 86, 7210–7254, 1981. 6980
López-Puertas, M., Funke, B., Gil-López, S., von Clarmann, T., Stiller, G. P., Höpfner, M., Kellmann, S., Mengistu Tsidu, G., Fischer, H., and Jackman, C. H.: HNO_3, N_2O_5, and $ClONO_2$ enhancements after the October-November 2003 solar proton events, J. Geophys. Res., 110, A09S44, doi:10.1029/2005JA011051, 2005a. 6991
López-Puertas, M., Funke, B., Gil-López, S., von Clarmann, T., Stiller, G. P., Kellmann, S., Fischer, H., and Jackman, C. H.: Observation of NO_x enhancement and ozone depletion in the Northern and Southern Hemispheres after the October-November 2003 solar proton events, J. Geophys. Res., 110, A09S43, doi:10.1029/2005JA011050, 2005b. 6991
Manney, G. L., Sabutis, J. L., Allen, D. R., Lahoz, W. A., Scaife, A. A., Randall, C., Pawson, S., Naujokat, B., and Swinbank, R.: Simulations of dynamics and transport during the September 2002 Antarctic major warming, J. Atmos. Sci., 62, 690–707, 2005. 6976
Manzini, E. and McFarlane, N. A.: The effect of varying the source spectrum of a gravity wave parameterization in a middle atmosphere general circulation model, J. Geophys. Res., 103, 31 523–31 539, 1998. 6968
Manzini, E., Giorgetta, M. A., Esch, M., Kornblueh, L., and Roeckner, E.: The influence of sea

surface temperatures on the Northern winter stratosphere: Ensemble simulations with the MAECHAM5 model, J. Climate, in press, 2006. 6961
Meilinger, S. K.: Heterogeneous Chemistry in the Tropopause Region: Impact of Aircraft Emissions, Ph.D. thesis, ETH Zürich, Switzerland, http://www.mpch-mainz.mpg.de/~smeili/diss/diss_new.ps.gz, 2000. 6963
Mengistu Tsidu, G., Stiller, G. P., von Clarmann, T., Funke, B., Höpfner, M., Fischer, H., Glatthor, N., Grabowski, U., Kellmann, S., Kiefer, M., Linden, A., López-Puertas, M., Milz, M., Steck, T., and Wang, D. Y.: NO_y from Michelson Interferometer for Passive Atmospheric Sounding on Environmental Satellite during the Southern Hemisphere polar vortex split in September/October 2002, J. Geophys. Res., 110, D11301, doi:10.1029/2004JD005322, 2005. 6976, 6990
Naujokat, B.: An update of the observed quasi-biennial oscillation of the stratospheric winds over the tropics, J. Atmos. Sci., 43, 1873–1877, 1986. 6965
Nordeng, T. E.: Extended versions of the convective parametrization scheme at ECMWF and their impact on the mean and transient activity of the model in the tropics, Tech. rep., ECWMF, 1994. 6961
Novelli, P. C., Masarie, K. A., and Lang, P. M.: Distributions and recent changes in carbon monoxide in the lower troposphere, J. Geophys. Res., 103, 19 015–19 033, 1998. 6981
Pawson, S., Kodera, K., Hamilton, K., Shepherd, T. G., Beagley, S. R., Boville, B. A., Farrara, J. D., Fairlie, T. D. A., Kitoh, A., Lahoz, W. A., Langematz, U., Manzini, E., Rind, D. H., Scaife, A. A., Shibata, K., Simon, P., Swinbank, R., Takacs, L., Wilson, R. J., Al-Saadi, J. A., Amodei, M., Chiba, M., Coy, L., de Grandpre, J., Eckman, R. S., Fiorino, M., Grose, W. L., Koide, H., Koshyk, J. N., Li, D., Lerner, J., Mahlman, J. D., McFarlane, N. A., Mechoso, C. R., Molod, A., O'Neill, A., Pierce, R. B., Randel, W. J., Rood, R. B., and Wu, F.: The GCM-reality intercomparison project for SPARC (GRIPS): Scientific issues and initial results, Bul. Am. Met. Soc., 81, 781–796, 2000. 6959
Pickering, K. E., Wang, Y., Tao, W.-K., Price, C., and Müller, J.-F.: Vertical distribution of lightning NO_x for use in regional and chemical transport models, J. Geophys. Res., 103, 31 203–31 216, 1998. 6963
Price, C. and Rind, D.: Modeling Global Lightning Distributions in a General Circulation Model, Mon. Weather Rev., 122, 1930–1939, 1994. 6963
Prinn, R. G., Weiss, R. F., Fraser, P. J., Simmonds, P. G., Cunnold, D. M., Alyea, F. N., O'Doherty, S., Salameh, P., Miller, B. R., Huang, J., Wang, R. H. J., Hartley, D. E., Harth,

C., Steele, L. P., Sturrock, G., Midgley, P. M., and McCulloch, A.: A history of chemically and radiatively important gases in air deduced from ALE/GAGE/AGAGE, J. Geophys. Res., 105, 17 751–17 792, 2000. 6966

Prinn, R. G., Huang, J., Weiss, R. F., Cunnold, D. M., Fraser, P. J., Simmonds, P. G., McCulloch, A., Harth, C., Salameh, P., O'Doherty, S., Wang, R. H. J., Porter, L., and Miller, B. R.: Evidence for substantial variations of atmospheric hydroxyl radicals in the past two decades, Science, 292, 1882–1888, 2001. 6986

Riese, M., Spang, P., Preusse, P., Ern, M., Jarisch, M., Offermann, D., and Grossmann, K. H.: Cryogenic Infrared Spectrometer and Telescopes for the Atmosphere (CRISTA) data processing and atmospheric temperature and trace gas retrieval, J. Geophys. Res., 104, 16 349–16 367, 1999. 6975

Roeckner, E., Bäuml, G., Bonaventura, L., Brokopf, R., Esch, M., Giorgetta, M., Hagemann, S., Kirchner, I., Kornblueh, L., Manzini, E., Rhodin, A., Schlese, U., Schulzweida, U., and Tompkins, A.: The atmospheric general circulation model ECHAM5. PART I: Model description, Tech. rep., Max Planck Institute for Meteorology, MPI-Report 349, http://www.mpimet.mpg.de/fileadmin/publikationen/Reports/max_scirep_349.pdf, 2003. 6959, 6961

Roeckner, E., Brokopf, R., Esch, M., Giorgetta, M., Hagemann, S., Kornblueh, L., Manzini, E., Schlese, U., and Schulzweida, U.: The atmospheric general circulation model ECHAM5. PART II: Sensitivity of Simulated Climate to Horizontal and Vertical Resolution, Tech. rep., Max Planck Institute for Meteorology, MPI-Report 354, http://www.mpimet.mpg.de/fileadmin/publikationen/Reports/max_scirep_354.pdf, 2004. 6959

Roeckner, E., Brokopf, R., Esch, M., Giorgetta, M., Hagemann, S., Kornblueh, L., Manzini, E., Schlese, U., and Schulzweida, U.: Sensitivity of simulated climate to horizontal and vertical resolution in the ECHAM5 atmosphere model, J. Climate, in press, 2006. 6961

Roelofs, G.-J. and Lelieveld, J.: Model study of the influence of cross-tropopause O_3 transports on tropospheric O_3 levels, Tellus, 49B, 38–55, 1997. 6980

Roelofs, G.-J. and Lelieveld, J.: Tropospheric ozone simulation with a chemistry general circulation model: Influence of higher hydrocarbon chemistry, J. Geophys. Res., 105, 22 697–22 712, 2000. 6959

Roesch, A. and Roeckner, E.: Assessment of snow cover and surface albedo in the ECHAM5 general circulation model, J. Climate, in press, 2006. 6961

Rudolf, B.: Satellite-based global precipitation estimates and validation results, Satellite Application Facility Workshop on Climate Monitoring, Dresden, Germany, Workshop Report,

Tech. rep., EUMETSAT, ISBN 92-9110-042-0, 2001. 6969
Sander, R., Kerkweg, A., Jöckel, P., and Lelieveld, J.: Technical Note: The new comprehensive atmospheric chemistry module MECCA, Atmos. Chem. Phys., 5, 445–450, 2005. 6963
Sandu, A. and Sander, R.: Technical Note: Simulating chemical systems in Fortran90 and Matlab with the kinetic preprocessor KPP-2.1, Atmos. Chem. Phys., 6, 187–195, 2006. 6963
Schmitt, A. and Brunner, B.: Emissions from aviation and their development over time, in: Pollutants from air traffic - results of atmospheric research 1992-1997. Final Report on the BMBF Verbundprogramm "Schadstoffe in der Luftfahrt", Tech. report, DLR – Mitteilung 97-04, 1–301, 1997. 6964
Spivakovsky, C. M., Yevich, R., Logan, J. A., Wofsy, S. C., McElroy, M. B., and Prather, M. J.: Tropospheric OH in a three-dimensional chemical tracer model: An assessment based on observations of CH_3CCl_3, J. Geophys. Res., 95, 18 441–18 471, 1990. 6985, 6986
Spivakovsky, C. M., Logan, J. A., Montzka, S. A., Balkanski, Y. J., Foreman-Fowler, M., Jones, D. B. A., Horowitz, L. W., Fusco, A. C., Brenninkmeijer, C. A. M., Prather, M. J., Wofsy, S. C., and McElroy, M. B.: Three-dimensional climatological distribution of tropospheric OH: Update and evaluation, J. Geophys. Res., 105, 8931–8980, 2000. 6986, 6987, 6988, 7017, 7018
Steil, B., Dameris, M., Brühl, C., Crutzen, P. J., Grewe, V., Ponater, M., and Sausen, R.: Development of a chemistry module for GCMs: First results of a multiannual integration, Ann. Geophys., 16, 205–228, 1998. 6963
Steil, B., Brühl, C., Manzini, E., Crutzen, P., Lelieveld, J., Rasch, P. J., Roeckner, E., and Krüger, K.: A new interactive chemistry climate model. I: Present day climatology and interannual variability of the middle atmosphere using the model and 9 years of HALOE/UARS data, J. Geophys. Res., 108, 4290, doi:10.1029/2002JD002971, 2003. 6959, 6962, 6966, 6973
Stevenson, D. S., Dentener, F. J., Schultz, M. G., Ellingsen, K., van Noije, T. P. C., Wild, O., Zeng, G., Amann, M., Atherton, C. S., Bell, N., Bergmann, D. J., Bey, I., Butler, T., Cofala, J., Collins, W. J., Derwent, R. G., Doherty, R. M., Drevet, J., Eskes, H. J., Fiore, A. M., Gauss, M., Hauglustaine, D. A., Horowitz, L. W., Isaksen, I. S. A., Krol, M. C., Lamarque, J.-F., Lawrence, M. G., Montanaro, V., Müller, J.-F., Pitari, G., Prather, M. J., Pyle, J. A., Rast, S., Rodriguez, J. M., Sanderson, M. G., Savage, N. H., Shindell, D. T., Strahan, S. E., Sudo, K., and Szopa, S.: Multimodel ensemble simulations of present-day and near-future tropospheric ozone, J. Geophys. Res., 111, D08301, doi:10.1029/2005JD006338, 2006. 6980, 6986
Stier, P., Feichter, J., Kinne, S., Kloster, S., Vignati, E., Wilson, J., Ganzeveld, L., Tegen, I.,

Werner, M., Balkanski, Y., Schulz, M., Boucher, O., Minikin, A., and Petzold, A.: The aerosol-climate model ECHAM5-HAM, Atmos. Chem. Phys., 5, 1125–1156, 2005. 6999

Stiller, G. P., Mengistu Tsidu, G., von Clarmann, T., Glatthor, N., Höpfner, M., Kellmann, S., Linden, A., Ruhnke, R., Fischer, H., López-Puertas, M., Funke, B., and Gil-López, S.: An enhanced HNO_3 second maximum in the Antarctic mid-winter upper stratosphere 2003, J. Geophys. Res., 110, D20303, doi:10.1029/2005JD006011, 2005. 6991

Tanre, D., Geleyn, J.-F., and Slingo, J. M.: First results of the introduction of an advanced aerosol-radiation interaction in the ECMWF low resolution global model, in: Aerosols and their climatic effects, edited by: Gerber, H. and Deepak, A., 133–177, A. Deepak, Hampton, VA, 1984. 6965

Taylor, K. E.: Summarizing multiple aspects of model performance in a single diagram, J. Geophys. Res., 106, 7183–7192, 2001. 7001

Thompson, A. M., Witte, J. C., McPeters, R. D., Oltmans, S. J., Schmidlin, F. J., Logan, J. A., Fujiwara, M., Kirchhoff, V. W. J. H., Psny, F., Coetzee, G. J. R., Hoegger, B., Kawakami, S., Ogawa, T., Johnson, B. J., Vömel, H., and Labow, G.: Southern Hemisphere Aditional Ozonesondes SHADOZ 1998–2000 tropical ozone climatology: Comparison with Total Ozone Mapping Spectrometer (TOMS) and ground-based measurements, J. Geophys. Res., 108, 8238, doi:10.1029/2001JD000967, 2003a. 6988

Thompson, A. M., Witte, J. C., Oltmans, S. J., Schmidlin, F. J., Logan, J. A., Fujiwara, M., Kirchhoff, V. W. J. H., Posny, F., Coetzee, G. J. R., Hoegger, B., Kawakami, S., Ogawa, T., Fortuin, J. P. F., and Kelder, H. M.: Southern Hemisphere Aditional Ozonesondes SHADOZ 1998–2000 tropical ozone climatology: 2. Tropospheric variability and the zonal wave-one, J. Geophys. Res., 108, 8241, doi:10.1029/2002JD002241, 2003b. 6988

Tiedtke, M.: A comprehensive mass flux scheme for cumulus parametrization in large-scale models, Mon. Weather Rev., 117, 1779–1800, 1989. 6961

Tost, H.: Global Modelling of Cloud, Convection and Precipitation Influences on Trace Gases and Aerosols, Ph.D. thesis, University of Bonn, Germany, 2006. 6985, 6998

Tost, H., Jöckel, P., Kerkweg, A., Sander, R., and Lelieveld, J.: Technical Note: A new comprehensive SCAVenging submodel for global atmospheric chemistry modelling, Atmos. Chem. Phys., 6, 565–574, 2006a. 6965

van Aalst, M. K., van den Broek, M. M. P., Bregman, A., Brühl, C., Steil, B., Toon, G. C., Garcelon, S., Hansford, G. M., Jones, R. L., Gardiner, T. D., Roelofs, G.-J., Lelieveld, J., and Crutzen, P. J.: Trace gas transport in the 1999/2000 Arctic; comaparison of nudged GCM

runs with observations, Atmos. Chem. Phys., 4, 81–93, 2004. 6960
van Aardenne, J. A., Dentener, F., Olivier, J. G. G., Peters, J. A. H. W., and Ganzeveld, L. N.: The EDGAR3.2 Fast Track 2000 dataset (32FT2000), Tech. rep., Joint Research Centre, Institute for Environment and Sustainability (JRC-IES), Climate Change Unit, TP280, 21020, Ispra (Va), Italy, http://www.mnp.nl/edgar/model/v32ft2000edgar/docv32ft2000/, 2005. 6960
van Noije, T. P. C., Eskes, H. J., Dentener, F. J., Stevenson, D. S., Ellingsen, K., Schultz, M. G., Wild, O., Amann, M., Atherton, C. S., Bergmann, D. J., Bey, I., Boersma, K. F., Butler, T., Cofala, J., Drevet, J., Fiore, A. M., Gauss, M., Hauglustaine, D. A., Horowitz, L. W., Isaksen, I. S. A., Krol, M. C., Lamarque, J.-F., Lawrence, M. G., Martin, R. V., Montanaro, V., Müller, J.-F., Pitari, G., Prather, M. J., Pyle, J. A., Richter, A., Rodriguez, J. M., Savage, N. H., Strahan, S. E., Sudo, K., Szopa, S., and van Roozendael, M.: Multi-model ensemble simulations of tropospheric NO_2 compared with GOME retrievals for the year 2000, Atmos. Chem. Phys. Discuss., 6, 2965–3047, 2006. 6983
Vignati, E., Wilson, J., and Stier, P.: M7: An efficient size-resolved aerosol microphysics module for large-scale aerosol transport models, J. Geophys. Res., 109, D22202, doi:10.1029/2003JD004485, 2004. 6999
von Clarmann, T., Chidiezie Chineke, T., Fischer, H., Funke, B., García-Comas, M., Gil-López, S., Glatthor, N., Grabowski, U., Höpfner, M., Kellmann, S., Kiefer, M., Linden, A., López-Puertas, M., López-Valverde, M. Á., Mengistu Tsidu, G., Milz, M., Steck, T., and Stiller, G. P.: Remote Sensing of the Middle Atmosphere with MIPAS, in: Remote Sensing of Clouds and the Atmosphere VII, Proceedings of SPIE Vol. 4882, SPIE, Bellingham, WA, USA, edited by: Schäfer, K., Lado-Bordowsky, O., Comerón, A., and Picard, R. H., 172–183, 2003a. 6973
von Clarmann, T., Glatthor, N., Grabowski, U., Höpfner, M., Kellmann, S., Kiefer, M., Linden, A., Mengistu Tsidu, G., Milz, M., Steck, T., Stiller, G. P., Wang, D. Y., Fischer, H., Funke, B., Gil-López, S., , and López-Puertas, M.: Retrieval of temperature and tangent altitude pointing from limb emission spectra recorded from space by the Michelson Interferometer for Passive Atmospheric Sounding (MIPAS), J. Geophys. Res., 108, 4736, doi:10.1029/2003JD003602, 2003b. 6973
von Kuhlmann, R.: Photochemistry of Tropospheric Ozone, its Precursors and the Hydroxyl radical: A 3D-Modeling Study Considering Non-Methane Hydrocarbons, PhD, University of Mainz, Germany, 2001. 6986, 6987, 7017, 7018
von Kuhlmann, R. and Lawrence, M. G.: The impact of ice uptake of nitric acid on atmospheric chemistry, Atmos. Chem. Phys., 6, 225–235, 2006. 6984

von Kuhlmann, R., Lawrence, M. G., Crutzen, P. J., and Rasch, P. J.: A model for studies of tropospheric ozone and non-methane hydrocarbons: Model evaluation of ozone related species, J. Geophys. Res., 108, 4729, doi:10.1029/2002JD003348, 2003a. 6984, 6985

von Kuhlmann, R., Lawrence, M. G., Crutzen, P. J., and Rasch, P. J.: A model for studies of tropospheric ozone and nonmethane hydrocarbons: Model description and ozone results, J. Geophys. Res., 108D, doi:10.1029/2002JD002893, 2003b. 6963, 6980

Wang, D. Y., von Clarmann, T., Fischer, H., Funke, B., Gil-López, S., Glatthor, N., Grabowski, U., Höpfner, M., Kaufmann, M., Kellmann, S., Kiefer, M., Koukouli, M. E., Linden, A., López-Puertas, M., Mengistu Tsidu, G., Milz, M., Steck, T., Stiller, G. P., Simmons, A. J., Dethof, A., Swinbank, R., Marquardt, C., Jiang, J. H., Romans, L. J., Wickert, J., Schmidt, T., Russell III, J., and Remsberg, E.: Validation of stratospheric temperatures measured by Michelson Interferometer for Passive Atmospheric Sounding MIPAS on Envisat, J. Geophys. Res., 110, D08301, doi:10.1029/2004JD005342, 2005. 6973

Wild, M. and Roeckner, E.: Radiative fluxes in the ECHAM5 general circulation model, J. Climate, in press, 2006. 6961

WMO: International meteorological vocabulary, 1992. 6966

Table 1. Annual stratospheric (tropopause to 10 hPa) ozone budget (S1 simulation) (production P, loss L) in Tg (average ± inter-annual standard deviation for the years 2000, 2001, 2003 and 2004). Values are rounded to Tg. The loss terms refer to the catalytic cycles involving families of reactive species.

	NH		SH		Global	
P,	6377	97	6393	101	12 770	176
L, odd oxygen	−579	4	−592	8	−1170	9
L, odd nitrogen	−3310	92	−3335	89	−6646	165
L, odd hydrogen	−1284	20	−1290	22	−2574	41
L, chlorine	−562	9	−656	19	−1219	21
L, bromine	−65	1	−102	5	−167	6
P_{net}	577	18	418	20	995	28

Table 2. Annual tropospheric ozone budget (S1 simulation) in Tg (average ± inter-annual standard deviation for the years 2000 to 2004). RO_2 comprises $C_2H_5O_2$, $CH_3C(O)OO$, $C_3H_7O_2$, $CH_3CH(O_2)CH_2OH$, $CH_3COCH_2O_2$, $C_4H_9O_2$, MVKO2, MEKO2, and ISO2. Values are rounded to Tg.

	NH		SH		Global	
$NO + HO_2$	1884	9	1244	8	3129	10
$NO + RO_2$	381	2	201	6	582	5
$NO + CH_3O_2$	685	4	459	3	1143	4
P	2949	15	1904	12	4854	14
$O_3 + OH$	−311	4	−221	4	−531	2
$O_3 + HO_2$	−823	5	−565	10	−1389	6
$H_2O + O(^1D)$	−1452	24	−1095	7	−2547	24
L	−2586	29	−1881	17	−4467	28
net	363	27	23	8	386	29
dry deposition	−508	4	−272	2	−780	4
change in burden	−1	7	0	6	0	10
STT[a]	144	25	249	10	393	25
burden	171	4	149	4	319	7
STT of $O_3^{(s)}$	676	23	522	10	1198	28
burden of $O_3^{(s)}$	78	4	59	3	137	5

[a]Net, derived by budget closure, accounts also for upward transport.

Table 3. Global simulated (S1) tropospheric NO_y budget in Tg(N)/year. The annual residuals (sources + sinks) are balanced by the stratospheric source.

	1998	1999	2000	2001	2002	2003	2004
Sources							
Prescribed Surface Emissions	43.10	43.10	43.10	43.10	43.10	43.10	43.10
Prescribed Aircraft Emissions	0.59	0.59	0.59	0.59	0.59	0.59	0.59
Online Emissions	7.01	6.78	6.77	6.81	6.87	6.84	6.81
Lightning	2.27	2.23	2.16	2.20	2.11	2.16	2.20
SUM	52.97	52.70	52.62	52.70	52.67	52.69	52.70
Sinks							
Precipitation Scavenging	−24.73	−24.32	−24.35	−24.29	−24.22	−24.21	−24.12
Dry Deposition: Nitrate	−16.56	−16.92	−16.80	−16.83	−16.89	−16.65	−16.78
Dry Deposition: NO_x	−3.20	−3.29	−3.32	−3.30	−3.24	−3.34	−3.34
Sedimentation: Aerosol Nitrate	−8.68	−8.59	−8.76	−8.80	−8.79	−8.94	−8.89
SUM	−53.17	−53.12	−53.23	−53.22	−53.14	−53.14	−53.13
Sources+Sinks	−0.20	−0.42	−0.61	−0.52	−0.47	−0.45	−0.43

Table 4. Global average OH concentration (in $10^6\,cm^{-3}$) calculated with different weighting factors. Listed are the five-year averages of the reference simulation (S1). The difference between 5 individual annual averages is less than $0.01\times10^6\,cm^{-3}$. The last row lists the global average methane lifetime ($\tau(CH_4)$ in years).

year	S1 2000–2004	S2000[a]	MATCH[b]
mass	1.08	1.14	0.95
volume	1.03	1.10	0.87
k_{MCF}	1.28	1.29	1.16
k_{CH_4}	1.31	1.32	1.19
$\tau(CH_4)$	8.02	8.23	9.12

[a] Spivakovsky et al. (2000)
[b] von Kuhlmann (2001)

ACPD
6, 6957–7050, 2006

EGU

Table 5. Mass weighted regional average OH concentration (in 10^6 cm^{-3}) of the reference simulation (S1). The vertical regions are denoted as follows: LT: Below 750 hPa; MT: 750–500 hPa; UT: 500–250 hPa; UT/TTL: 250 hPa – tropopause.

Region	REF(2000)	S2000[a]	MATCH[b]
LT, 90 S–30 S	0.54	0.47	0.51
LT, 30 S–0	1.84	1.44	1.51
LT, 0–30 N	2.05	1.52	1.76
LT, 30 N–90 N	0.82	0.76	0.86
MT, 90 S–30 S	0.55	0.72	0.46
MT, 30 S–0	1.50	2.00	1.48
MT, 0–30 N	1.65	1.99	1.61
MT, 30 N–90 N	0.70	0.88	0.72
UT, 90 S–30 S	0.48	0.64	0.36
UT, 30 S–0	1.01	1.43	0.82
UT, 0–30 N	1.07	1.36	0.96
UT, 30 N–90 N	0.55	0.64	0.52
UT/TTL,30 S–0	1.12		
UT/TTL,0–30 N	1.14		
Global	1.07	1.14	0.95

[a] Spivakovsky et al. (2000)
[b] von Kuhlmann (2001)

ACPD
6, 6957–7050, 2006

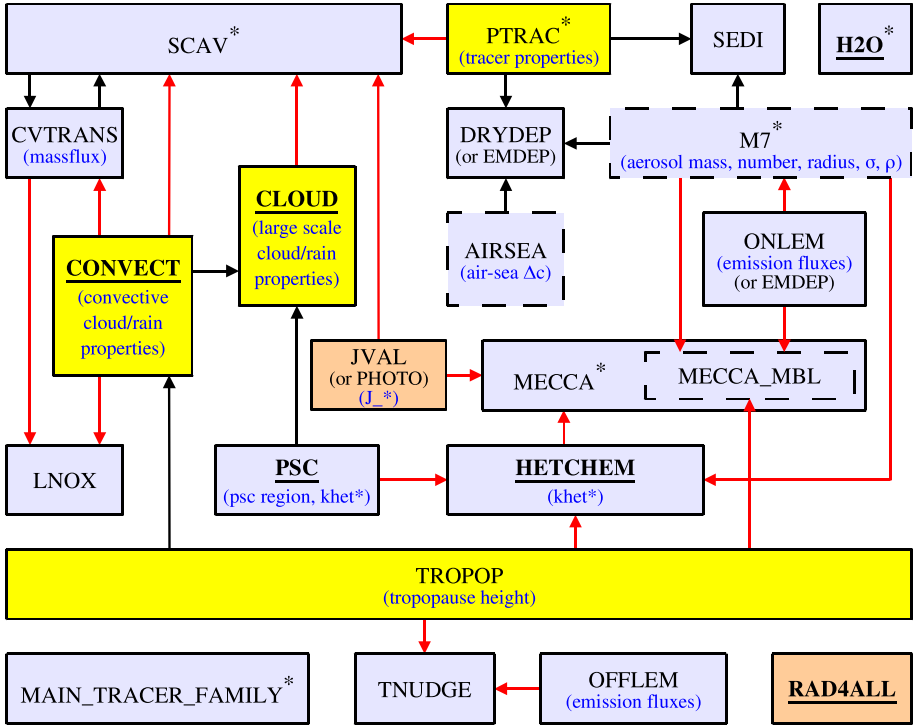

Fig. 1. Diagram of the coupling between submodels. The arrows indicate the data flow. Red arrows denote connections that can be controlled via namelists. Submodels in dashed boxes are switched off in the current model simulation. The colour of the boxes shows the effect on tracers. Yellow submodels do not change the tracer tendencies directly. Orange submodels use tracer values but do not change them. Blue submodels use tracers and also change their tendencies. Submodels with an asterisk define new tracers. Most submodels import data (e.g., temperature, humidity, pressure) from the ECHAM5 basemodel via the basemodel interface layer. Those with feedbacks to the basemodel are underlined (see text).

ACPD
6, 6957–7050, 2006

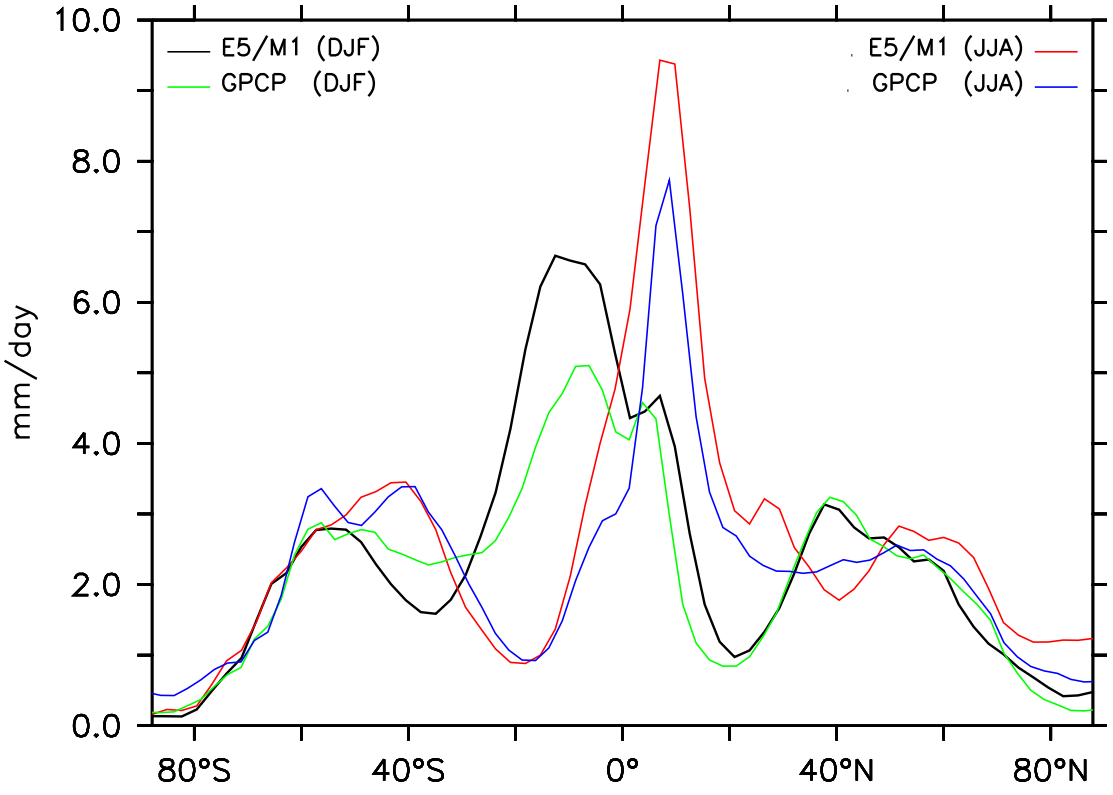

Fig. 2. Zonally averaged distributions of simulated (E5/M1, S1) and observed (GPCP) precipitation for DJF and JJA.

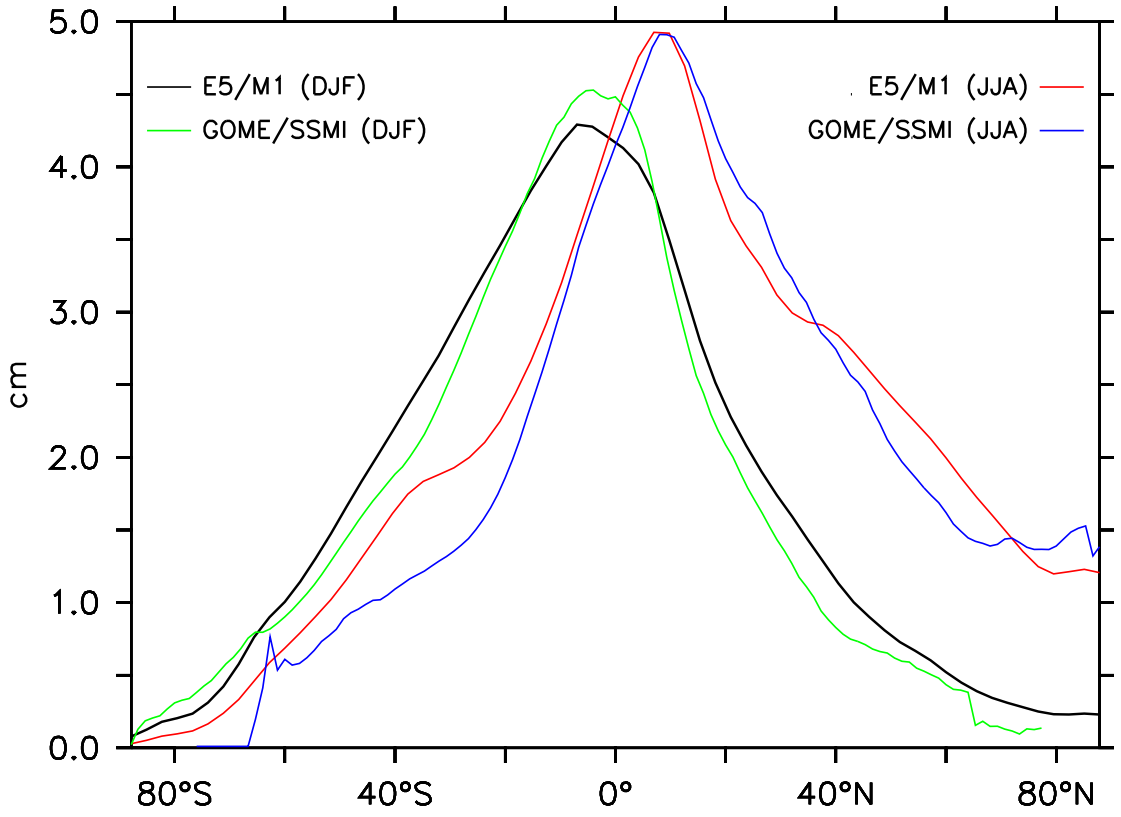

Fig. 3. Zonally averaged distributions of the simulated (E5/M1, S1) and observed (GOME/SSMI) water vapour column for DJF and JJA.

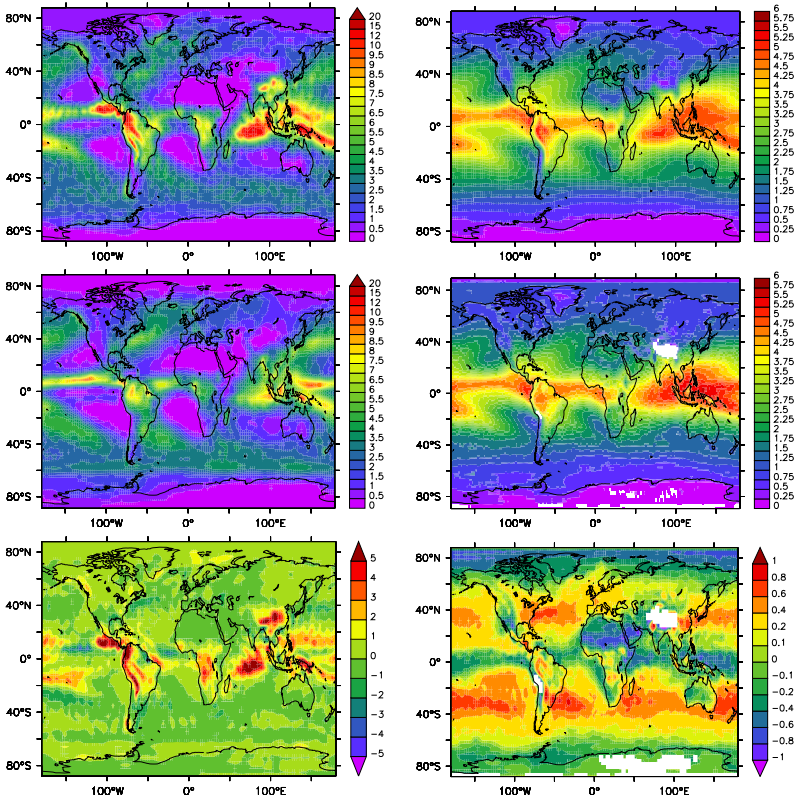

Fig. 4. Annual average simulated (S1, upper) and observed (middle) precipitation (mm/day, left) and water vapour (cm, right) for the years 1999 to 2002. The lower row shows the respective differences (E5/M1 (S1) minus observations).

ACPD
6, 6957–7050, 2006

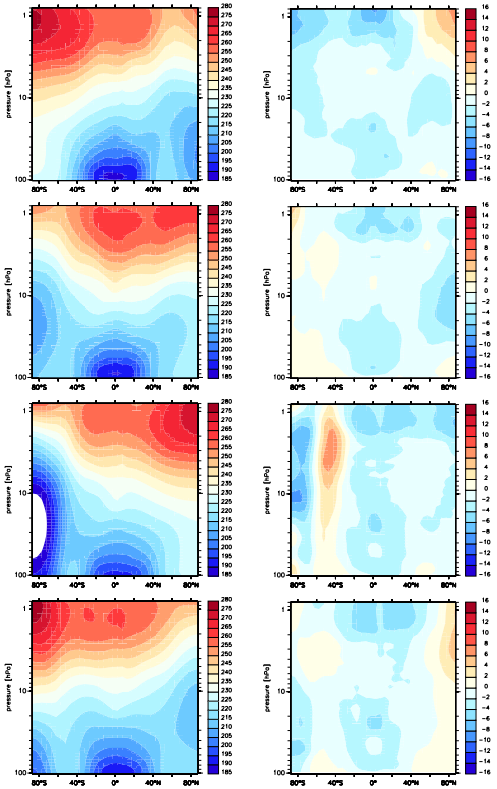

Fig. 5. Zonal averages of the temperature (in K) from the simulations (left) and the difference to observations (E5/M1 minus MIPAS, right). The seasons are DJF (2002/2003), MAM, JJA, and SON (2003) from top to bottom. DJF is from S1, all others from S2. The MIPAS datasets typically represent 15 days with about 14 orbits each.

ACPD
6, 6957–7050, 2006

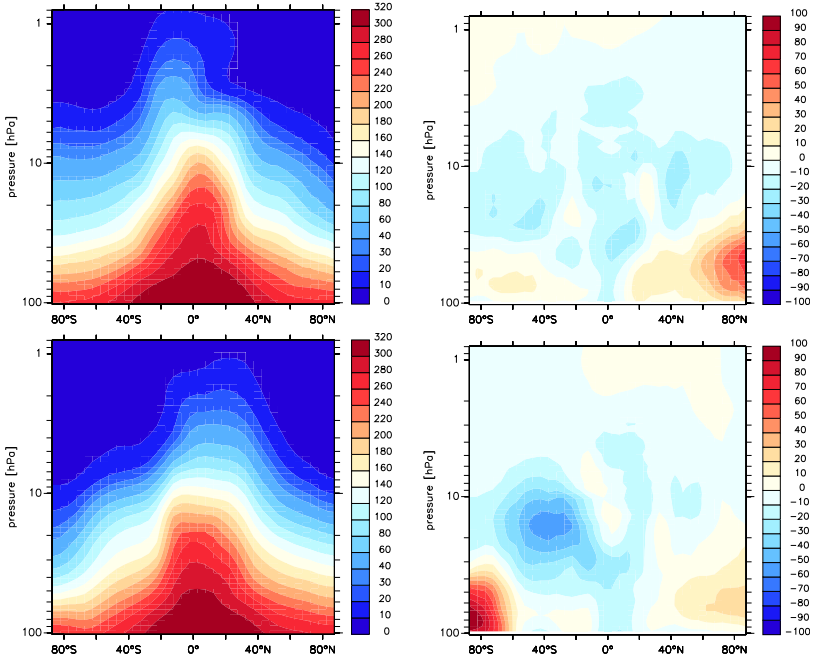

Fig. 6. Zonal averages of simulated (left) nitrous oxide (nmol/mol) and difference (model minus MIPAS) to observations (right). Top: DJF, S1; Bottom: SON, S2. The datasets typically represent 15 days with about 14 orbits each.

ACPD
6, 6957–7050, 2006

EGU

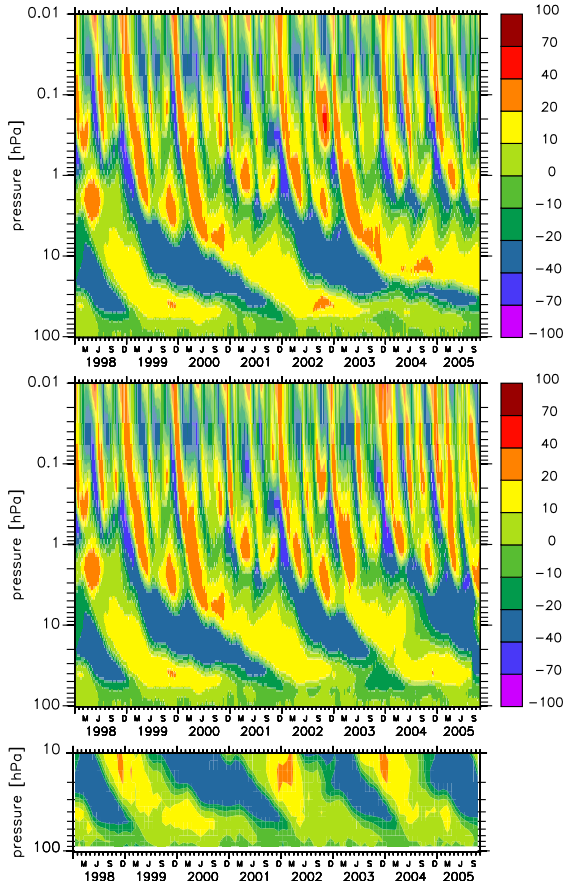

Fig. 7. Tropical zonal wind (in m/s) average between 2° S and 2° N) and its quasi-biennial oscillation (top panel: reference simulation (S1), middle panel: S1 with overlayed sensitivity studies (S2), lower panel: observations).

ACPD
6, 6957–7050, 2006

EGU

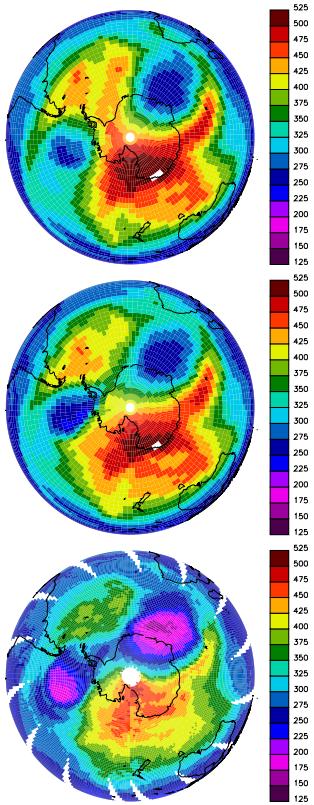

Fig. 8. Total ozone (in DU) on 26 September 2002 as simulated by E5/M1 (S1 in upper, and S2 in middle panel, respectively), and as observed by TOMS (lower panel).

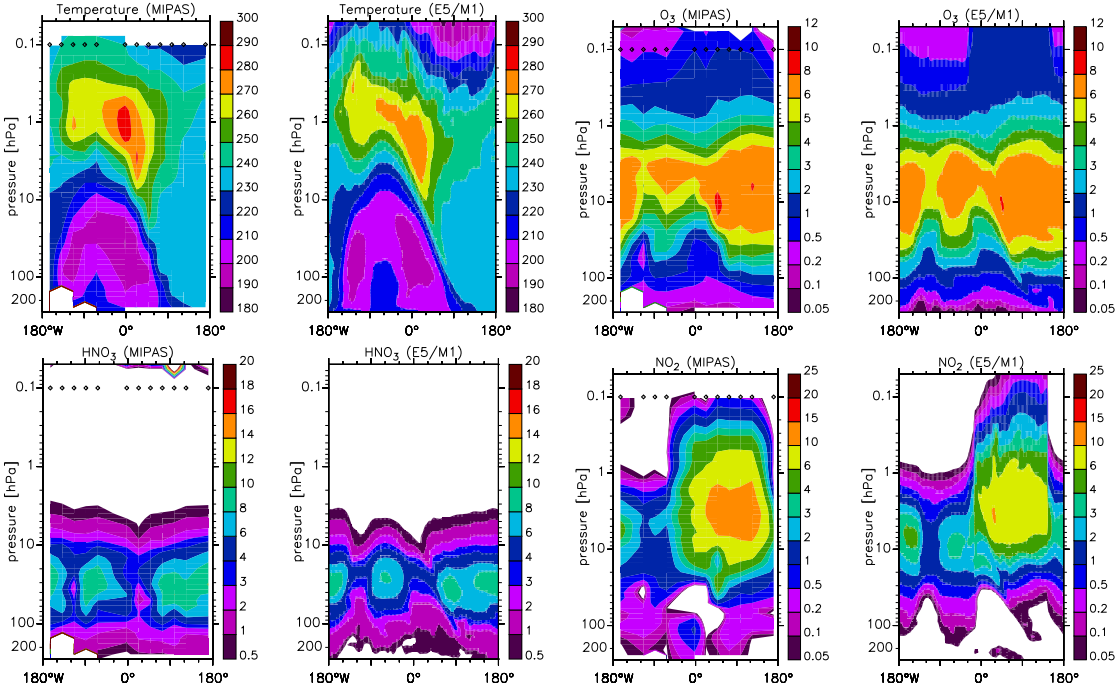

Fig. 9. MIPAS observations and model simulations (E5/M1, S1) of temperature (K), ozone (µmol/mol), HNO_3 (nmol/mol), and NO_2 (nmol/mol) for 22 September 2002, at 63° S. Between about 30° W and 150° E is night. Diamonds mark longitudes of measurements.

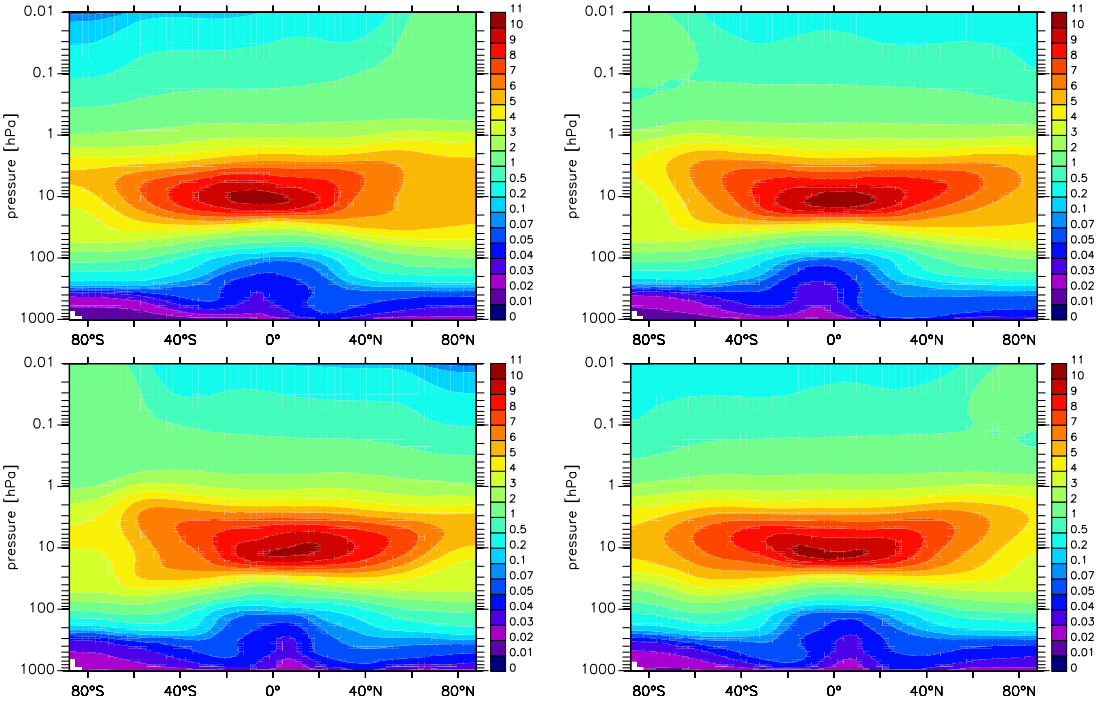

Fig. 10. 4-year-averages (2000-2004, excluding 2002) of calculated (S1) ozone (µmol/mol) for the 4 seasons (DJF: upper left; MAM: upper right; JJA: lower left; SON: lower right).

ACPD
6, 6957–7050, 2006

EGU

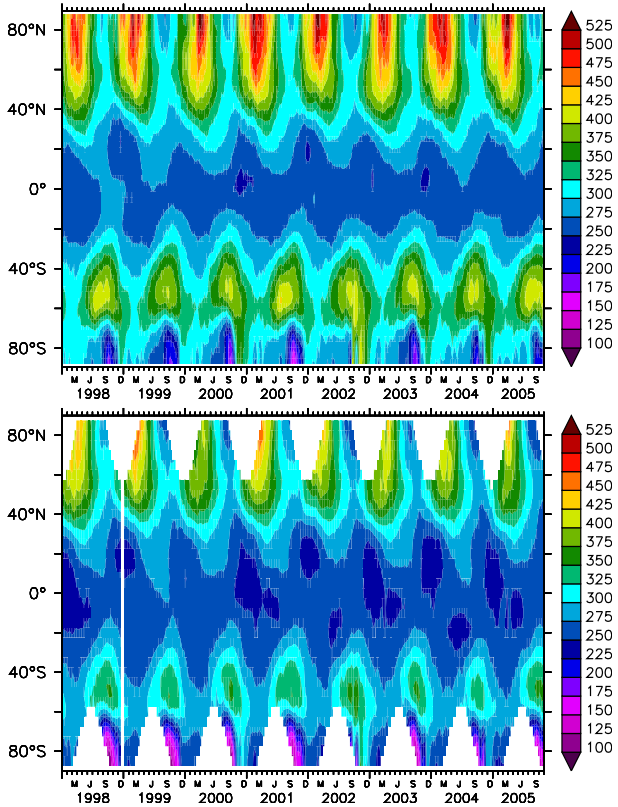

Fig. 11. Total ozone (DU), based on 10-day zonal averages for 8 years (upper panel: E5/M1 (S1), lower panel: TOMS satellite data).

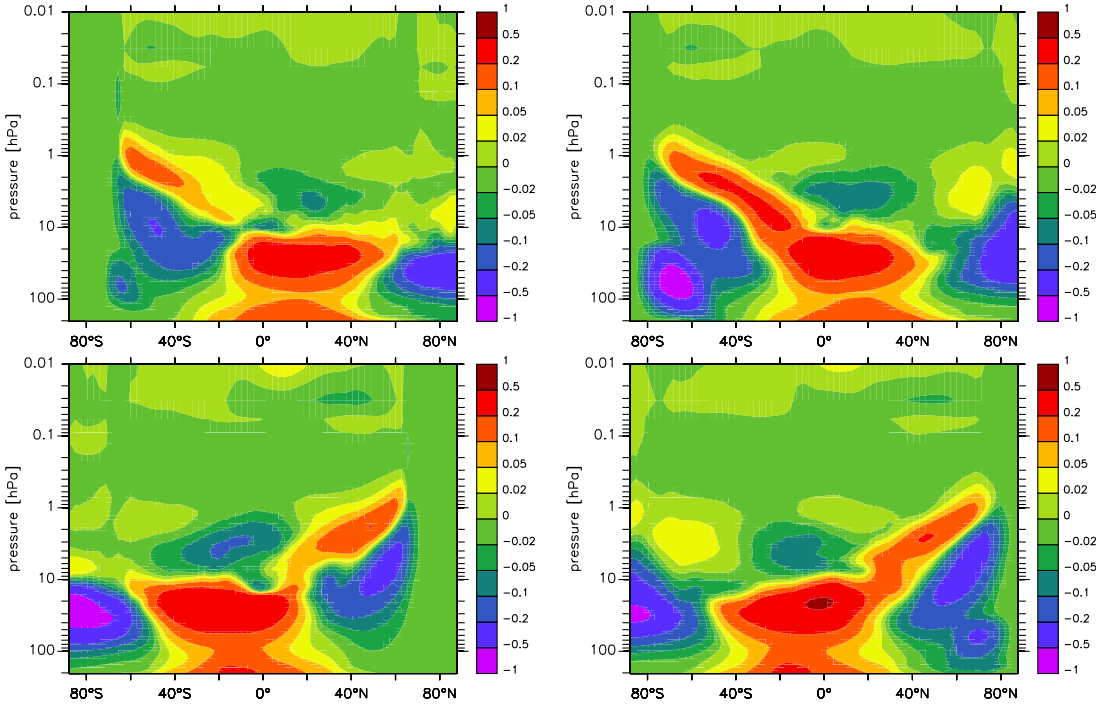

Fig. 12. Net chemical ozone production ($P_{net}=P-L$) with P being the chemical production from photolysis of molecular oxygen and L being the chemical loss due to the different catalytic cycles (odd nitrogen, oxygen, chlorine, bromine and hydrogen); June (upper left), August (upper right), December (lower left), and February (lower right). Shown are monthly diurnal averages for the year 2000 (S1) in 10^6 molecules/cm^3/s.

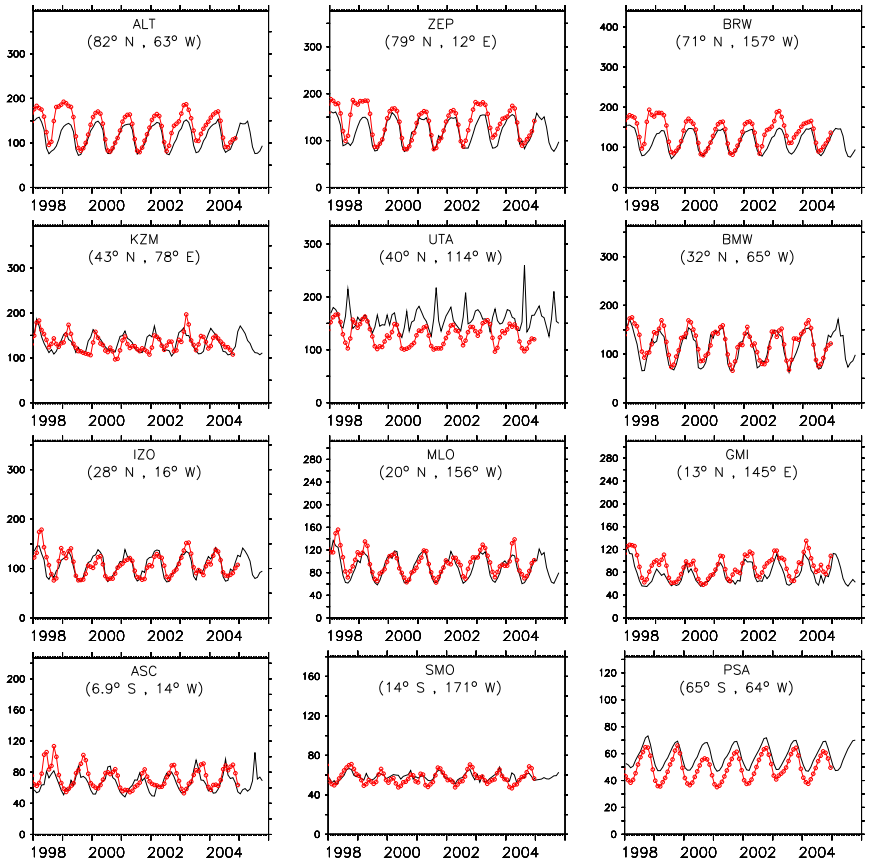

Fig. 13. Comparison of simulated (S1, black) and observed (red) CO mixing ratios (in nmol/mol) for selected NOAA/CMDL sites (from north to south).

ACPD
6, 6957–7050, 2006

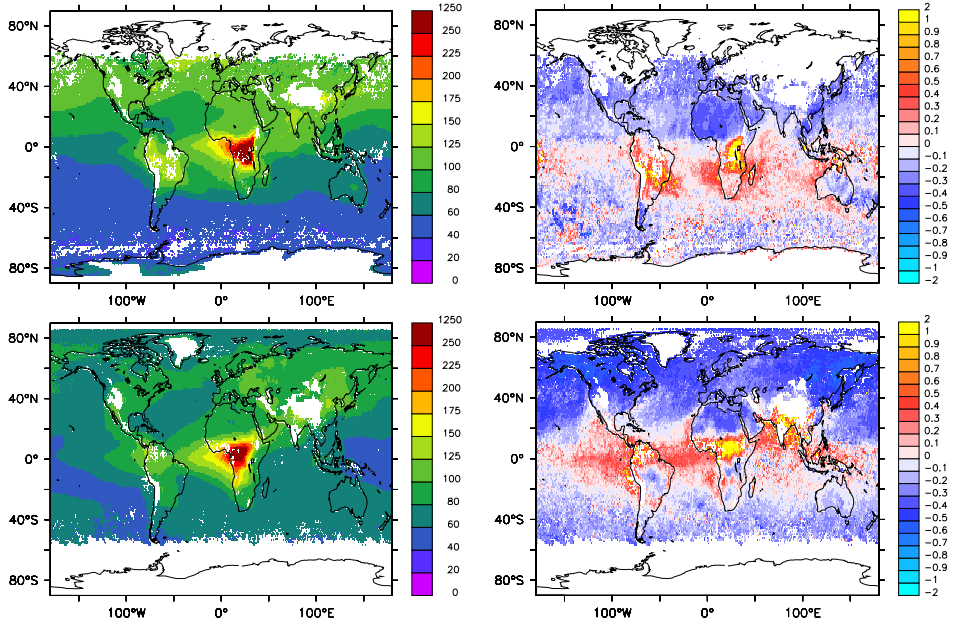

Fig. 14. Left: model calculated (S1) CO (in nmol/mol) at 700 hPa on the MOPITT kernel for January (top) and July (bottom) 2003. Right: relative difference (E5/M1-MOPITT/MOPITT) between the model simulation S1 and MOPITT for January (top) and July (bottom) 2003; positive values indicate that E5/M1 is higher and vice versa. Only daylight conditions have been considered.

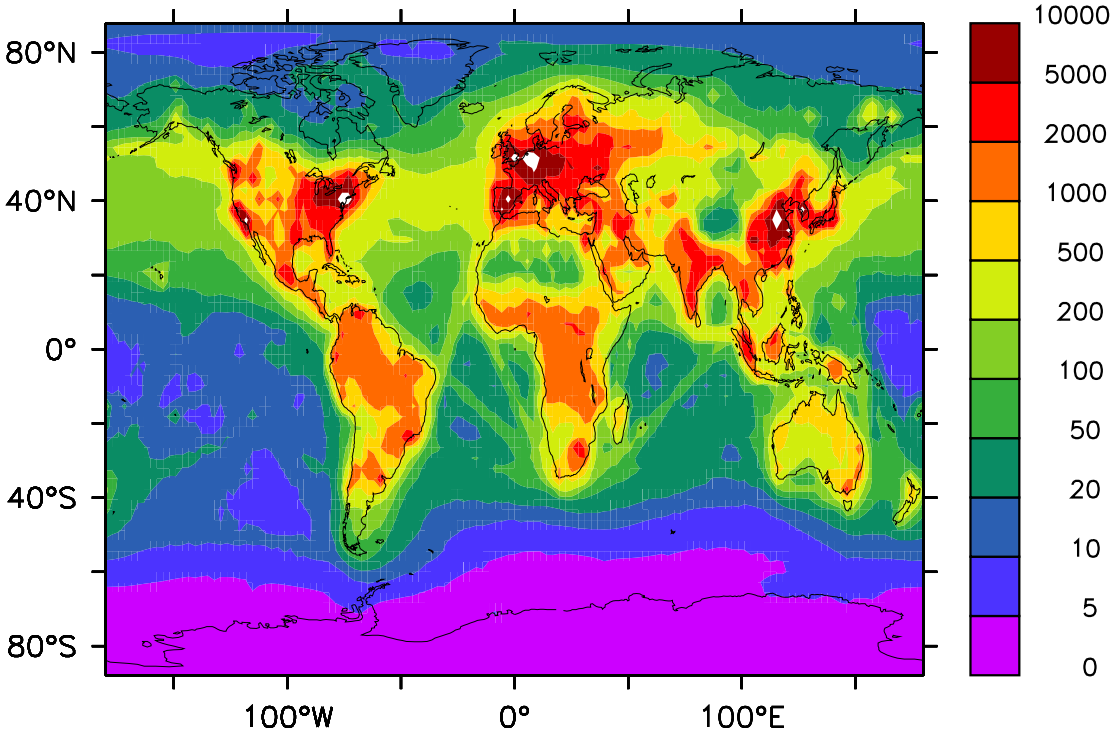

Fig. 15. Simulated (S1) 5-year mean surface NO_x distribution (pmol/mol).

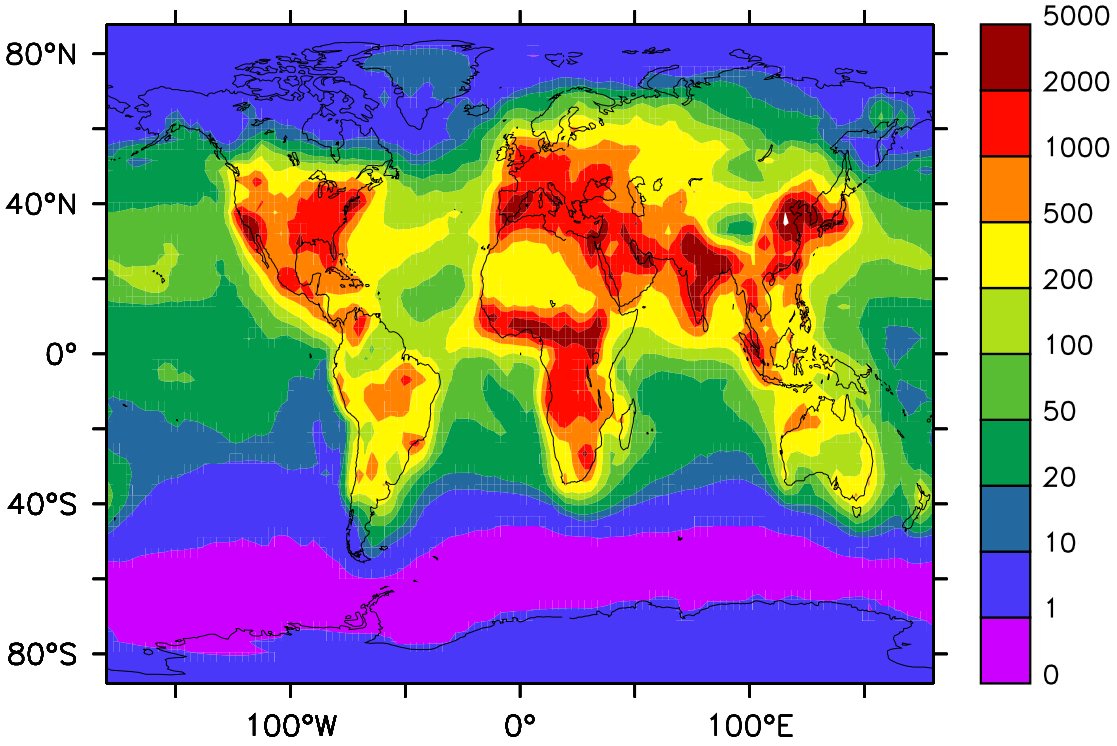

Fig. 16. Simulated (S1) 5-year mean surface HNO_3 distribution (pmol/mol).

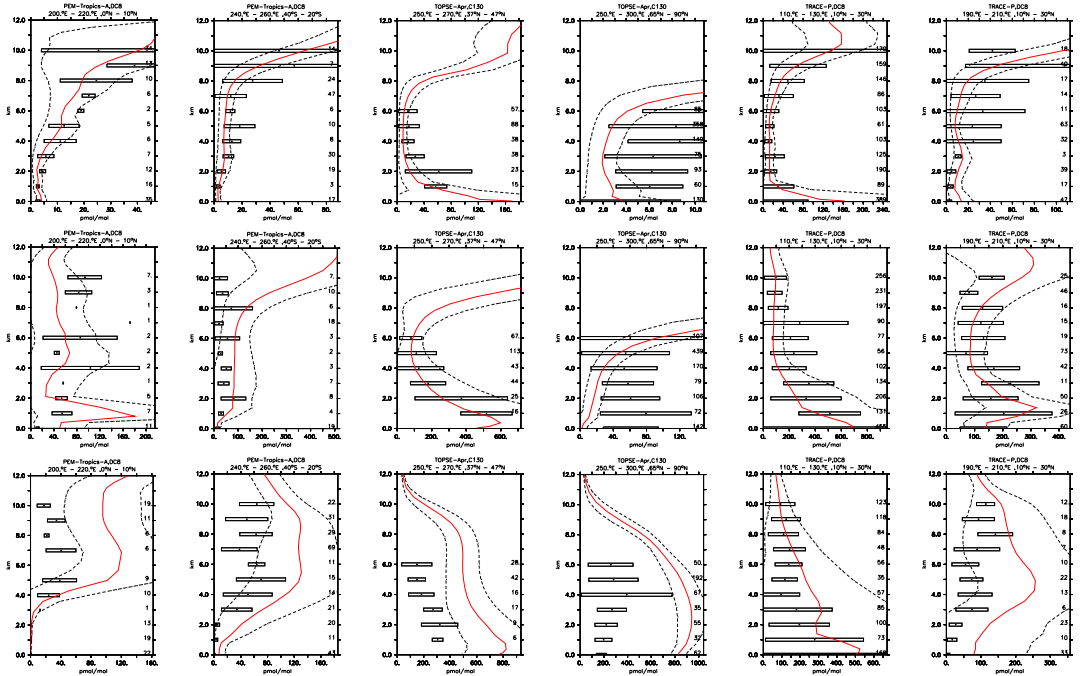

Fig. 17. Profiles (in pmol/mol) of NO (top), HNO_3 (middle), and PAN (bottom) for the simulated year 2000 (S1) compared to composite data for selected regions from Emmons et al. (2000). The bars show the standard deviation of the measurements, the asterixes show the averages, the red lines the model results, and the black dashed lines the simulated standard deviations. The numbers close to the right vertical axes indicate the number of available measurements.

ACPD
6, 6957–7050, 2006

EGU

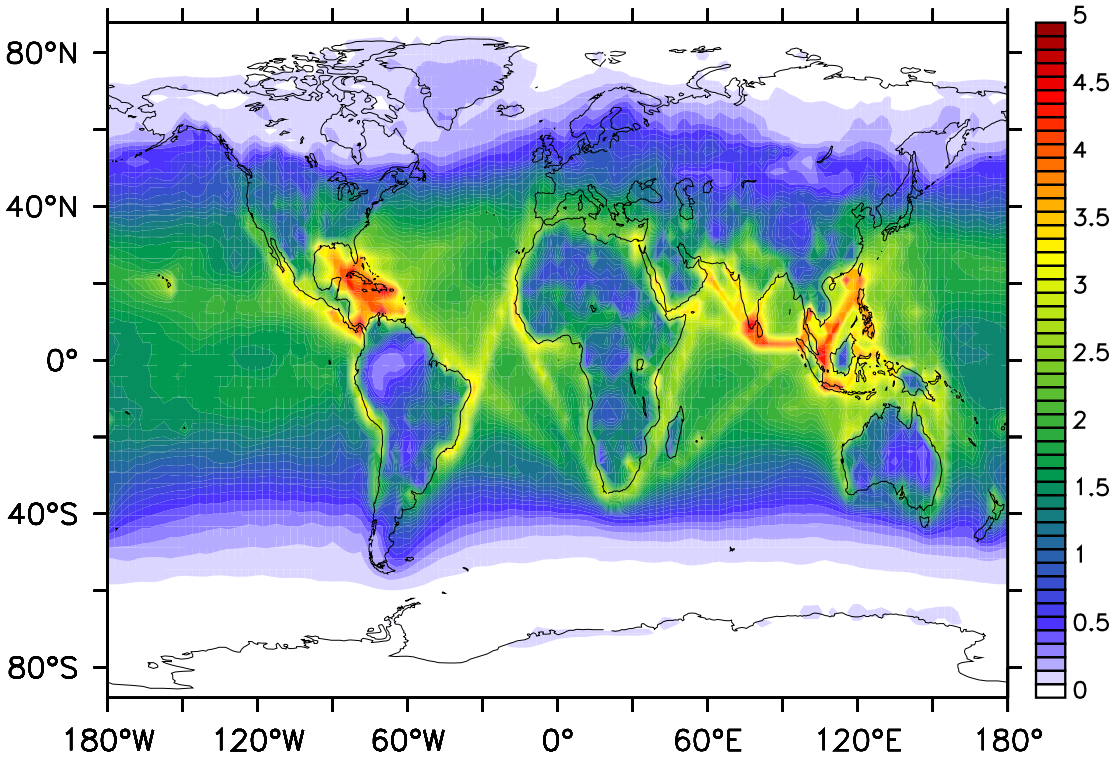

Fig. 18. 5-year average (2000 to 2004) of simulated (S1) diurnal mean OH ($10^6 cm^{-3}$) in the lowest model layer.

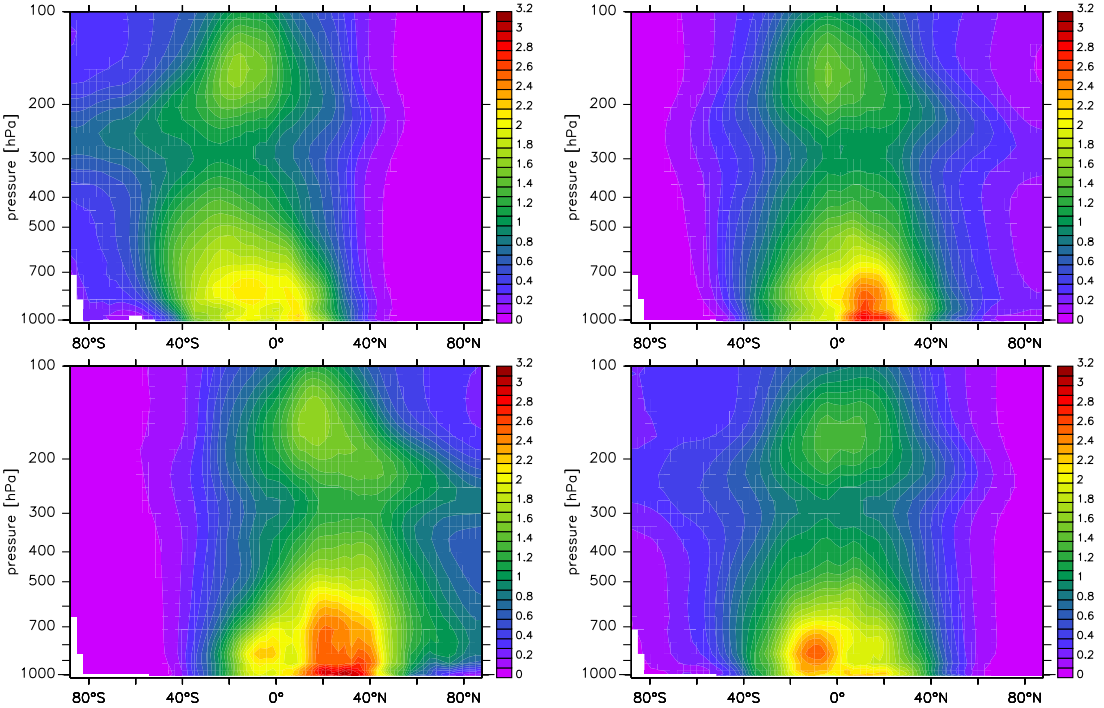

Fig. 19. 5-year averages (2000 to 2004) of simulated (S1) zonal and diurnal mean OH ($10^6 cm^{-3}$) for the 4 seasons (DJF: upper left; MAM: upper right; JJA: lower left; SON: lower right).

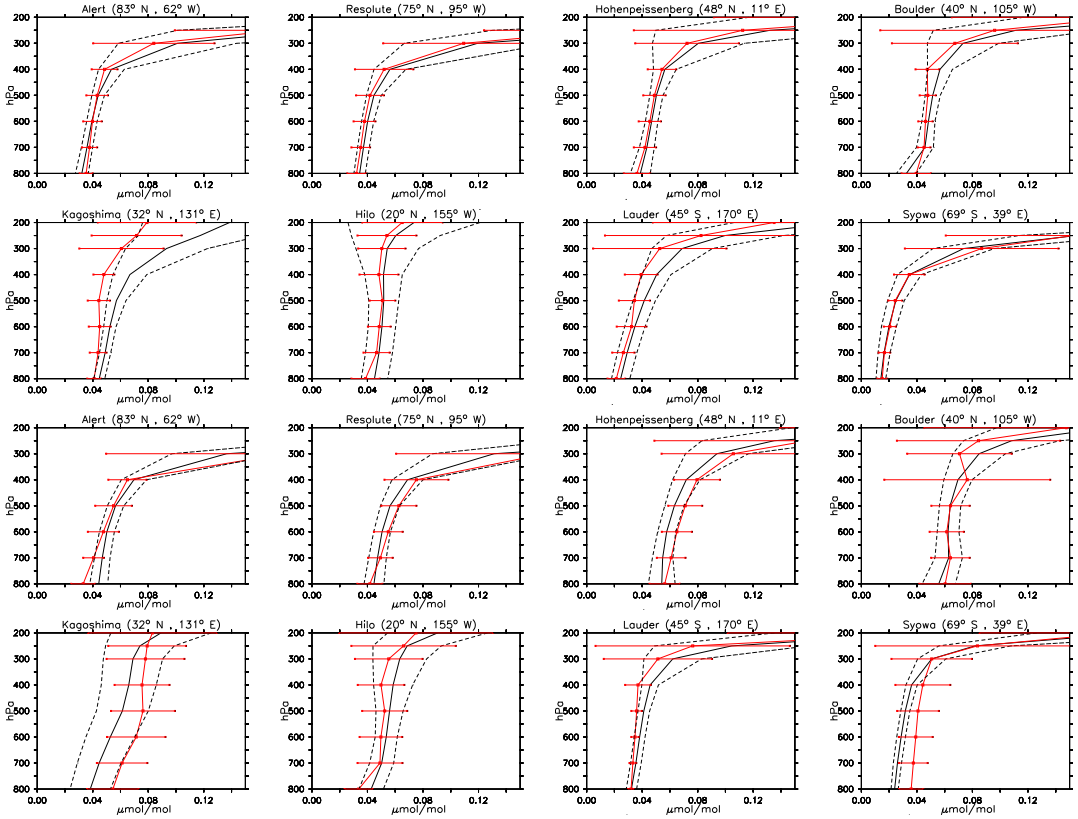

Fig. 20. Vertical profiles of ozone (in μmol/mol) in January (upper two rows) and June (lower two rows) in the free troposphere and tropopause region for selected sites from Logan (1999). Black lines are model results (7-year averages, S1) and red lines are observations. The dashed black lines show the model standard deviations, and the red bars the observed standard deviations.

ACPD
6, 6957–7050, 2006

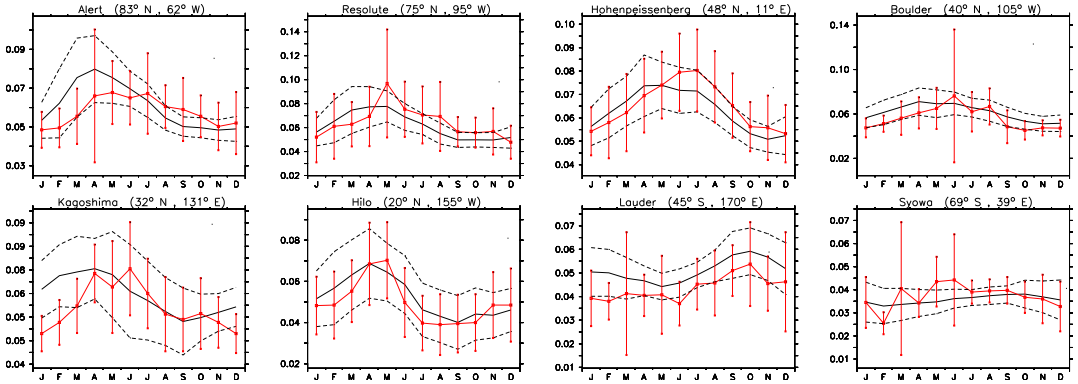

Fig. 21. Seasonal cycle of ozone (in µmol/mol) for selected sites from Logan (1999) in the troposphere at 400 hPa. Black lines are model results (7-year averages (1998–2004), S1) and red lines are observations. The dashed black lines show the model standard deviations, and the red bars the observed standard deviations.

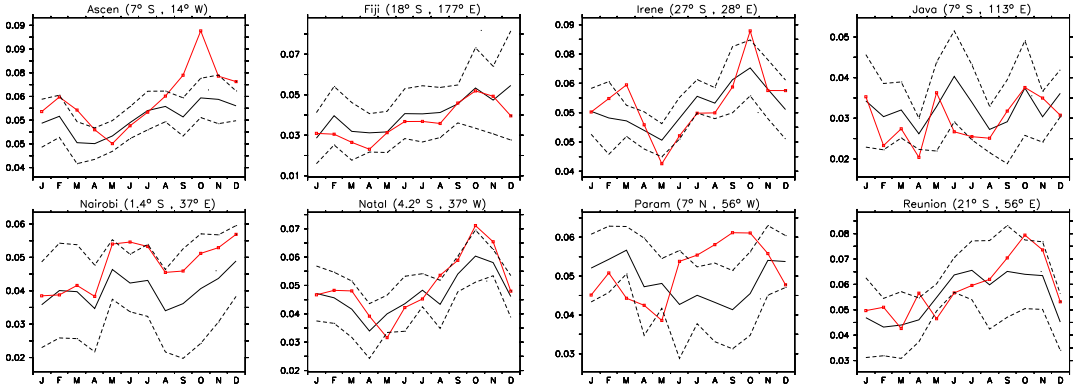

Fig. 22. Seasonal cycle of ozone (in µmol/mol) at 400 hPa obtained from the SHADOZ database (red) compared to the 7-year climatology (1998 to 2004) derived from the E5/M1 model simulation S1 (black). The dashed black lines show the model standard deviations.

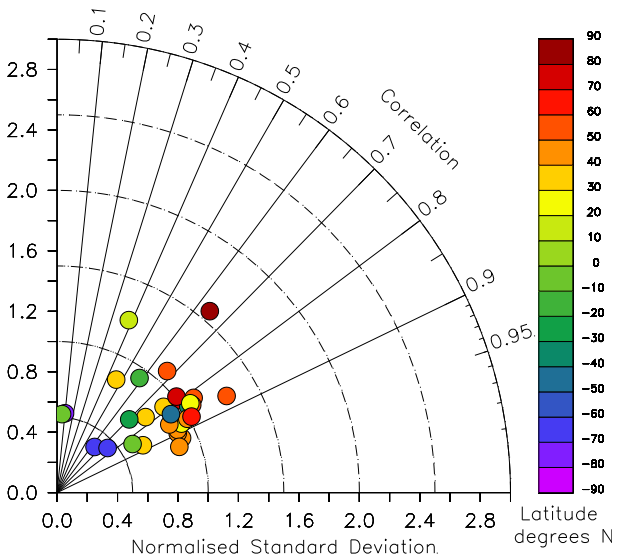

Fig. 23. Taylor plot of the correlation between observations and model results (S1) for the 400 hPa level for all sites from Logan (1999). The correlation has been error weighted (see Appendix C).

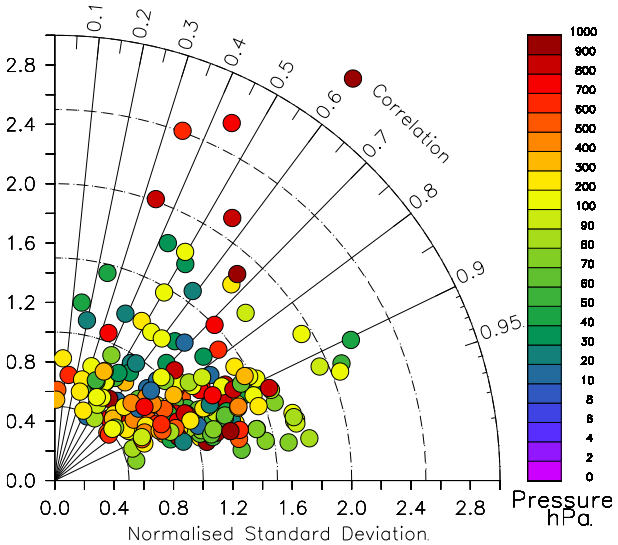

Fig. 24. Taylor plot of O_3 correlation between 7-year E5/M1 climatology (S1) and a similar climatology compiled from the SHADOZ database (see Sect. 5.4).

ACPD
6, 6957–7050, 2006

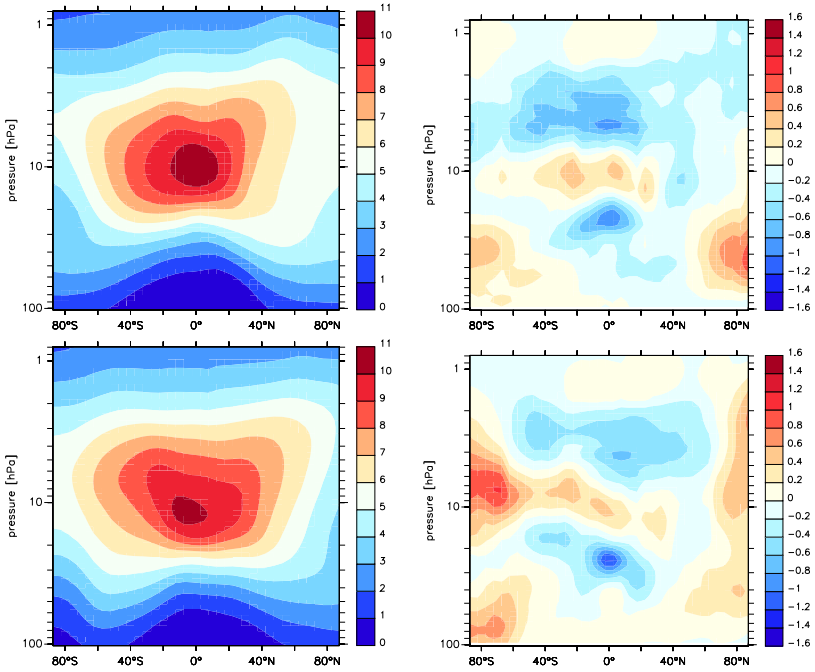

Fig. 25. Left: zonal averages of simulated ozone (in µmol/mol). Right: model minus MIPAS observations (in µmol/mol). Top: DJF, S1, Bottom SON, S2 with improved QBO. The datasets typically represent 15 days with about 14 orbits each.

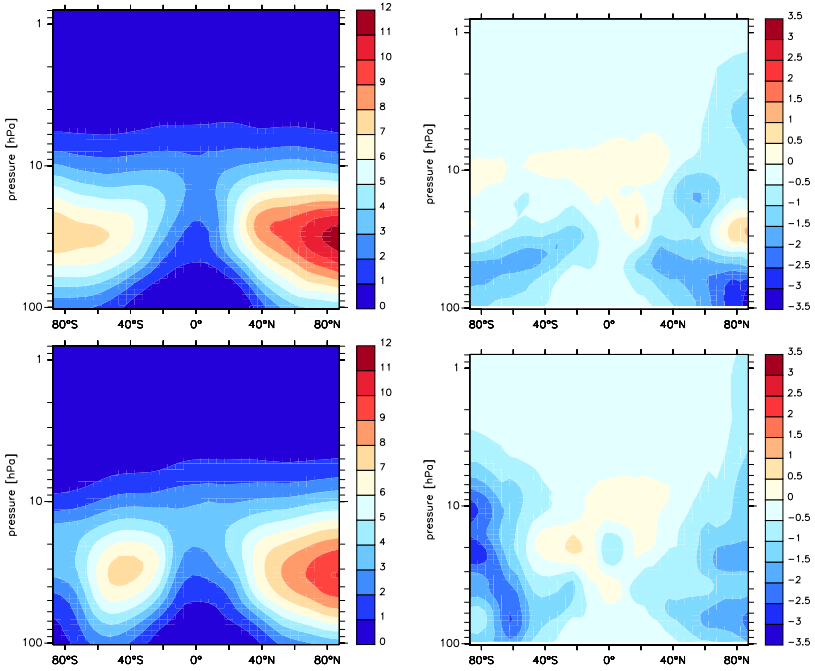

Fig. 26. Left: zonal averages of simulated HNO_3 (in nmol/mol). Right: model minus MIPAS observations (in nmol/mol). Top: DJF, S1, Bottom SON, S2. The datasets typically represent 15 days with about 14 orbits each.

ACPD
6, 6957–7050, 2006

EGU

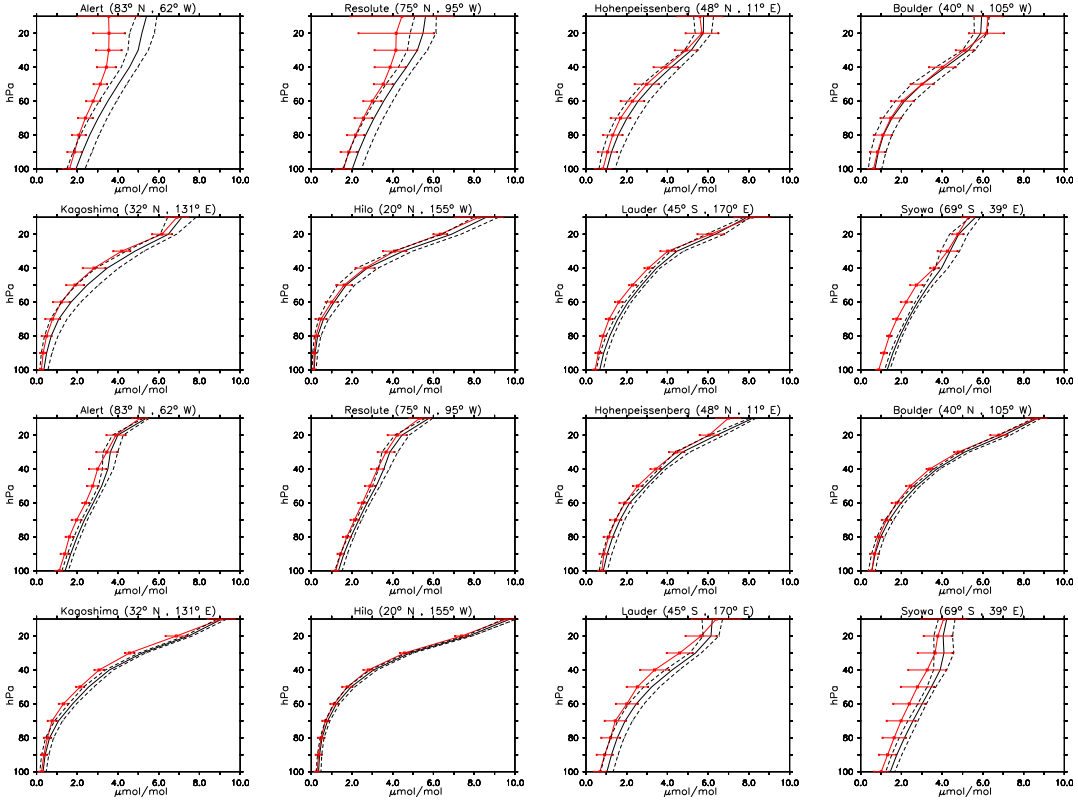

Fig. 27. Observed and simulated (S1) vertical profiles of ozone (in µmol/mol) for January (upper two rows) and June (lower two rows) in the stratosphere for selected sites from Logan (1999). Colours and line styles as in Fig. 20.

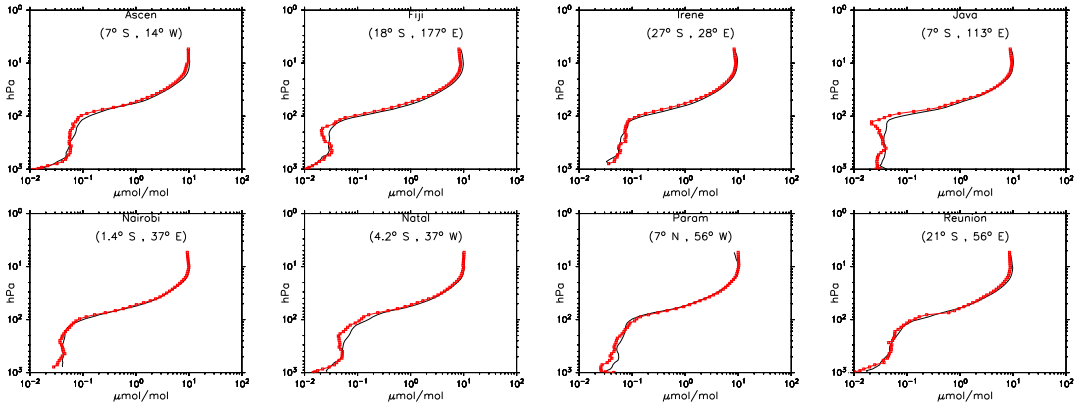

Fig. 28. Vertical profiles of ozone (in µmol/mol) for January for the sites from the SHADOZ database. Model climatology (S1) in black and measured climatology in red.

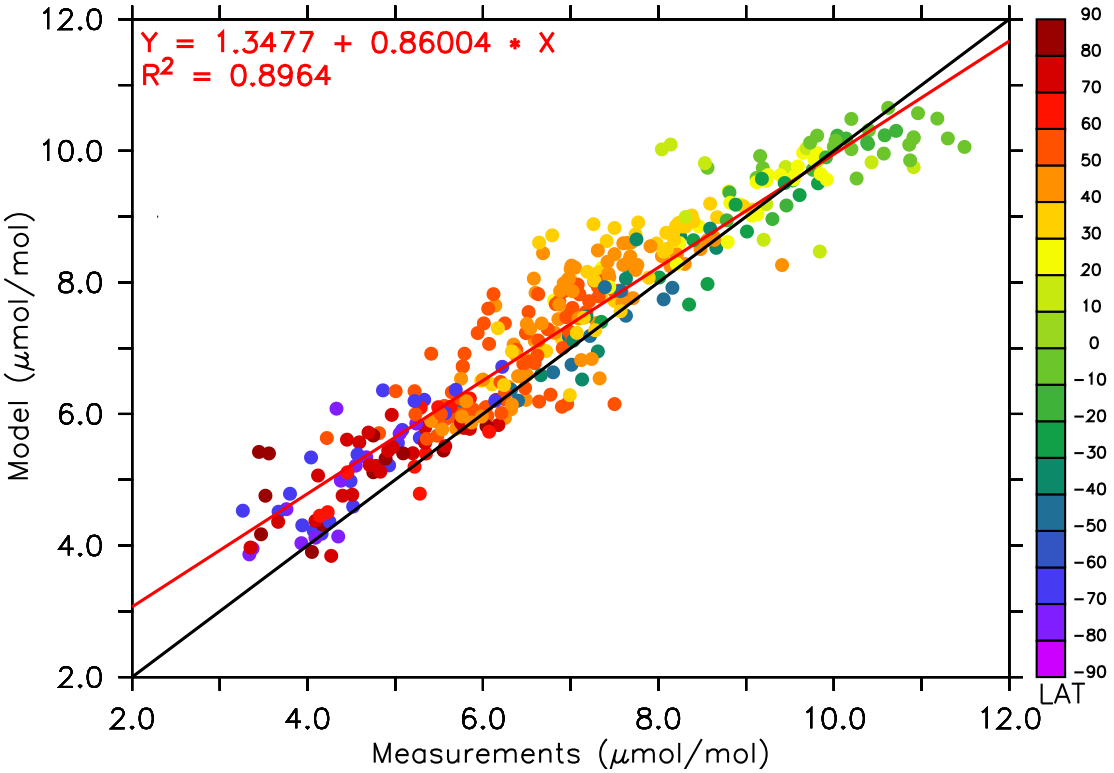

Fig. 29. Comparison of simulated (E5/M1, S1) and observed (Logan, 1999) vertical maximum O_3 mixing ratio (in µmol/mol). The colour code denotes the latitude.

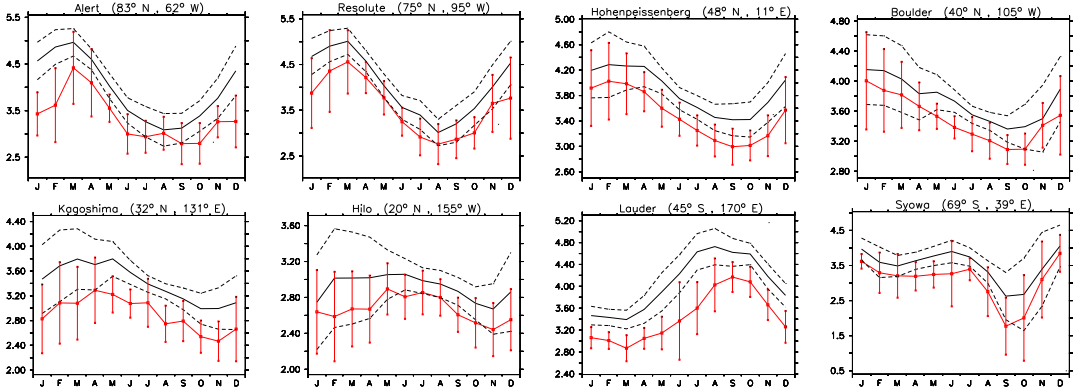

Fig. 30. Seasonal cycle of ozone (in µmol/mol) for selected sites from Logan (1999) in the stratosphere at 40 hPa. The model results (S1, black) represent a 7-year average.

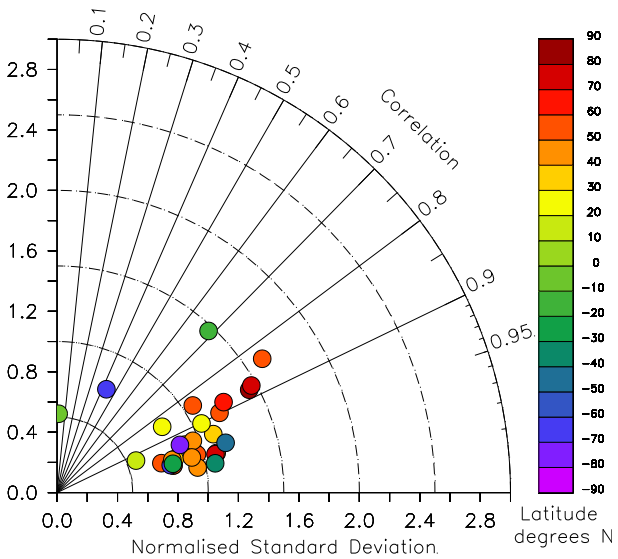

Fig. 31. Taylor plot of the correlation between observations and model results (S1) for the 40 hPa level for all sites from Logan (1999). The correlation has been error weighted (see Appendix C).

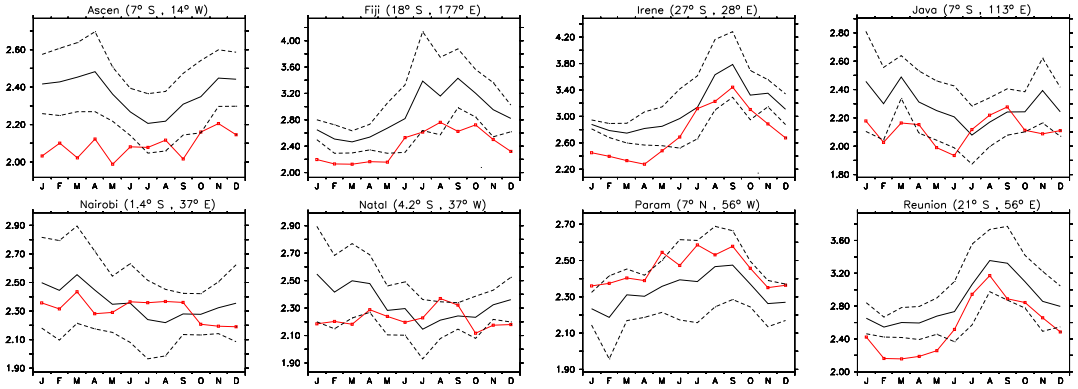

Fig. 32. Seasonal cycle of ozone (in µmol/mol) at 40 hPa obtained from the SHADOZ database (red) compared to the 7-year climatology (1998 to 2004) derived from the E5/M1 model simulation S1 (black).